

Iron and Ruthenium σ -Polyynyls of the General Formula $[\{M(dppe)Cp^*\}-(C\equiv C)_n-R]^{0/+}$ (M = Fe, Ru): An Experimental and Theoretical Investigation

Frédéric Gendron,[†] Alexandre Burgun,^{†,‡} Brian W. Skelton,^{§,||} Allan H. White,[§] Thierry Roisnel,[†] Michael I. Bruce,[‡] Jean-François Halet,[†] Claude Lapinte,^{*,†} and Karine Costuas^{*,†}

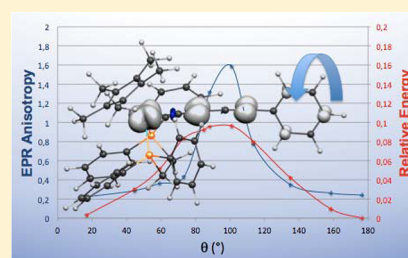
[†]Institut des Sciences chimiques de Rennes, UMR 6226 CNRS-Université de Rennes 1, Campus de Beaulieu, 35042 Rennes Cedex, France

[‡]School of Chemistry and Physics, University of Adelaide, South Australia 5005, Australia

[§]School of Chemistry and Biochemistry M313, University of Western Australia, Crawley, Western Australia 6009, Australia

Supporting Information

ABSTRACT: Two series of metal-polyynyl complexes of iron and ruthenium of general formula $[\{M(dppe)Cp^*\}-(C\equiv C)_n-R]^{0/+}$ (M = Fe, Ru; R = H, Ph, SiMe₃, Au(PPh₃); n = 1–3), have been synthesized, characterized, and theoretically analyzed. The results provide a comprehensive description of the effect of the length of the conjugated carbon chain and the role of the nature of the metal atom and the terminal substituent on their neutral and oxidized states. For the latter, the spin density found on the carbon chain is a source of instability; e.g., for R = Au(PPh₃), the oxidized compounds are much more accessible electrochemically than the rest of the series but are susceptible to radical attack. Of particular interest is the use of joint experimental and theoretical EPR studies, which allow elucidation of the differences of behavior within the two series. It reveals that the atomic spin density on the metal is not a sufficient criterion to evaluate EPR anisotropy but that the specific nodal properties of the frontier spin-orbitals highly influence the EPR components. The localization of the spin density on specific carbon atoms of the conjugated chain (even numbered) opens up the possibility of building extended systems by targeted radical reactions.



INTRODUCTION

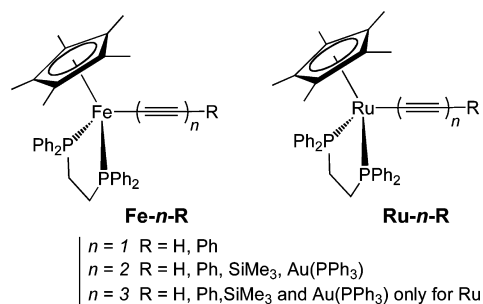
Due to the high reactivity of long all-carbon chains, the development of the chemistry of conjugated polyynes has been facilitated by stabilizing the chain with bulky end groups, often with metal fragments, or with protecting side ligands.¹ Nevertheless, synthesis of the oxidized parents, sufficiently stable to be characterized, remains difficult to access.¹ Such open-shell systems have high potential as conducting molecular wires or as building blocks toward larger functional molecules. In order to achieve this, the redox properties of the electron-rich Fe(dppe)Cp* and Ru(dppe)Cp* moieties have been used to stabilize different polyne chains. Here, for the first time, a series of substituted metal polyynyls containing diynyl to triynyl carbon chains have been characterized in their neutral and oxidized states (see Chart 1).

This comprehensive study was carried out with particular attention to the rationalization of the spin delocalization by a combined EPR and quantum chemical approach. The question of instability of the oxidized compounds was also studied experimentally and theoretically.

EXPERIMENTAL RESULTS

Syntheses and Characterization of Fe-2-Ph and Ru-2-Ph. As illustrated in Scheme 1, the iron and ruthenium derivatives were obtained by following different procedures.

Chart 1

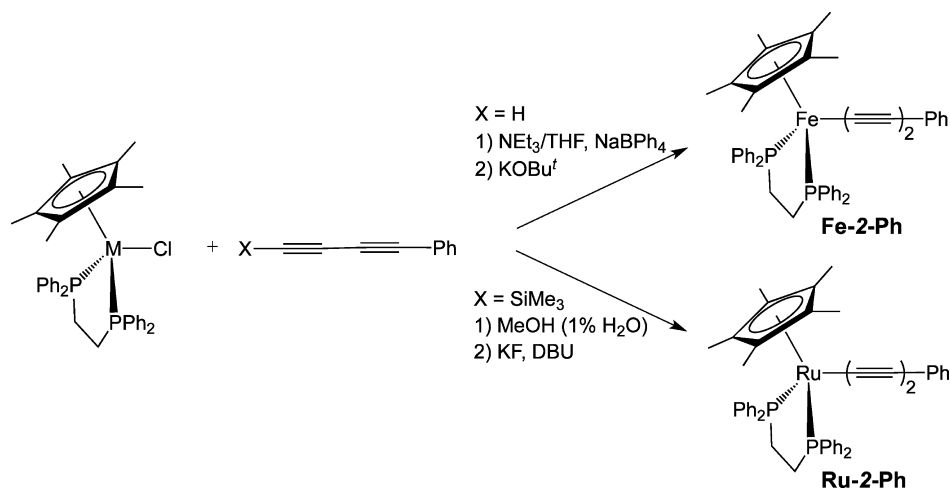


The iron complex $\{Fe(dppe)Cp^*\}-(C\equiv C)_2-Ph$ (**Fe-2-Ph**) was produced by treatment of $FeCl(dppe)Cp^*$ with 1 equiv of phenylbutadiyne in the presence of $NaBPh_4$ in triethylamine.² Before the solvent was removed under reduced pressure, an excess of $KOBu^t$ was added to prevent the formation of the butatrienyliene intermediate and thus subsequent decomposition. After extraction, **Fe-2-Ph** was isolated as an orange powder in 85% yield. When applied similarly to the ruthenium analogues, this described synthetic route did not give **Ru-2-Ph**

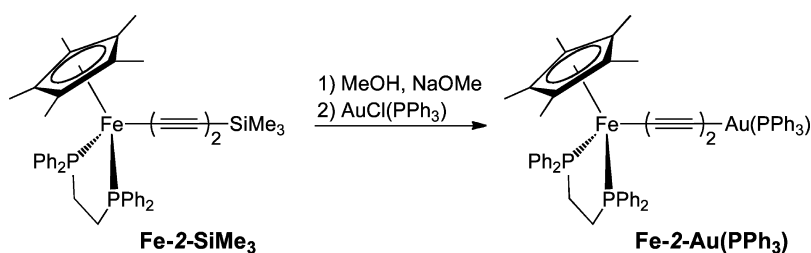
Received: June 26, 2012

Published: September 13, 2012

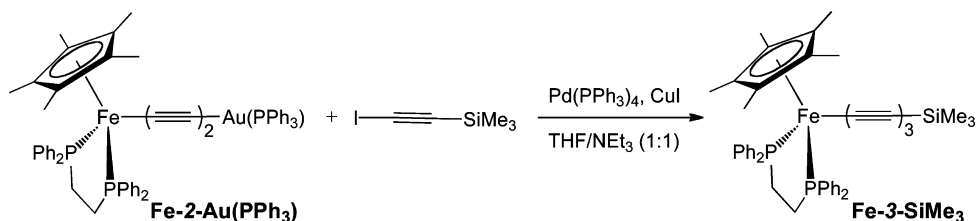
Scheme 1



Scheme 2



Scheme 3



(see Scheme 1). However, **Ru-2-Ph** can be obtained from the reaction between $\text{RuCl}(\text{dppe})\text{Cp}^*$ and $\text{PhC}\equiv\text{CC}\equiv\text{CSiMe}_3$ in methanol containing 1 equiv of KF , 1% of water, and a small amount of DBU .³ The complex **Ru-2-Ph** was isolated as a bright yellow powder in 87% yield. Satisfactory elemental analyses were obtained for these new complexes, which were also characterized by the usual spectroscopic methods and their structures confirmed by single-crystal X-ray studies (see below).

The IR spectrum of the new iron diyne complex **Fe-2-Ph** shows three $\nu(\text{C}\equiv\text{C})$ bands at 2150, 2007, and 1987 cm^{-1} , the lowest energy band being assigned to a Fermi resonance resulting from a coupling between a $\nu(\text{C}\equiv\text{C})$ mode with another vibration mode of the molecule, as previously observed for the alkynyl–iron derivatives.⁴ In accord with our assignment, the IR spectrum of **Ru-2-Ph** contains only two $\nu(\text{C}\equiv\text{C})$ bands at 2153 and 2016 cm^{-1} . The ^1H , ^{13}C , and ^{31}P NMR spectra of the two complexes are very similar. However, while for **Fe-2-Ph** the α -carbons of the diyne ligand are found as a triplet at $\delta 144.74\text{ ppm}$ ($^2J_{\text{CP}} = 38\text{ Hz}$), for **Ru-2-Ph** this resonance lies among the aromatic carbon resonances and cannot be assigned.

Synthesis and Characterization of Fe-2-Au(PPh₃). The heterobinuclear complex $\{\text{Fe}(\text{dppe})\text{Cp}^*\}-(\text{C}\equiv\text{C})_2-\text{Au}$

(PPh_3) (**Fe-2-Au(PPh₃)**) has been prepared by following a procedure similar to that previously developed for the ruthenium analogue $\{\text{Ru}(\text{dppe})\text{Cp}^*\}-(\text{C}\equiv\text{C})_2-\text{Au}(\text{PPh}_3)$ (**Ru-2-Au(PPh₃)**).⁵ Treatment of **Fe-2-SiMe₃** with sodium methoxide in a 1/1 THF/methanol mixture was followed by addition of 1 equiv of $\text{AuCl}(\text{PPh}_3)$ to the solution (Scheme 2). After 4 h of stirring, the precipitate was collected and washed with cold methanol to afford **Fe-2-Au(PPh₃)** as an orange solid.

The identity of the complex **Fe-2-Au(PPh₃)** was confirmed by an X-ray structure and by full spectroscopic characterization, including the four ^{13}C resonances of the carbon atoms of the chain, which were found at $\delta 88.84$, 94.18 , 104.06 , and 123.26 ppm ($t, ^2J_{\text{CP}} = 40\text{ Hz}$). The solution IR spectrum of **Fe-2-Au(PPh₃)** contains two $\nu(\text{C}\equiv\text{C})$ bands at 2069 and 1969 cm^{-1} , consistent with the asymmetry of the carbon bridge, as previously observed with other related heterobinuclear butadiynyl complexes.^{6,7}

Synthesis and Characterization of Fe-3-SiMe₃. The binuclear complexes $\{\text{Fe}(\text{dppe})\text{Cp}^*\}-(\text{C}\equiv\text{C})_3-\{\text{Fe}(\text{dppe})\text{Cp}^*\}$ (isolated as a mixture with its higher homologue $\{\text{Fe}(\text{dppe})\text{Cp}^*\}-(\text{C}\equiv\text{C})_4-\{\text{Fe}(\text{dppe})\text{Cp}^*\}$) and $\{\text{Fe}(\text{dppe})\text{Cp}^*\}-(\text{C}\equiv\text{C})_3-\{\text{Re}(\text{NO})(\text{PPh}_3)\text{Cp}^*\}$ constitute the only

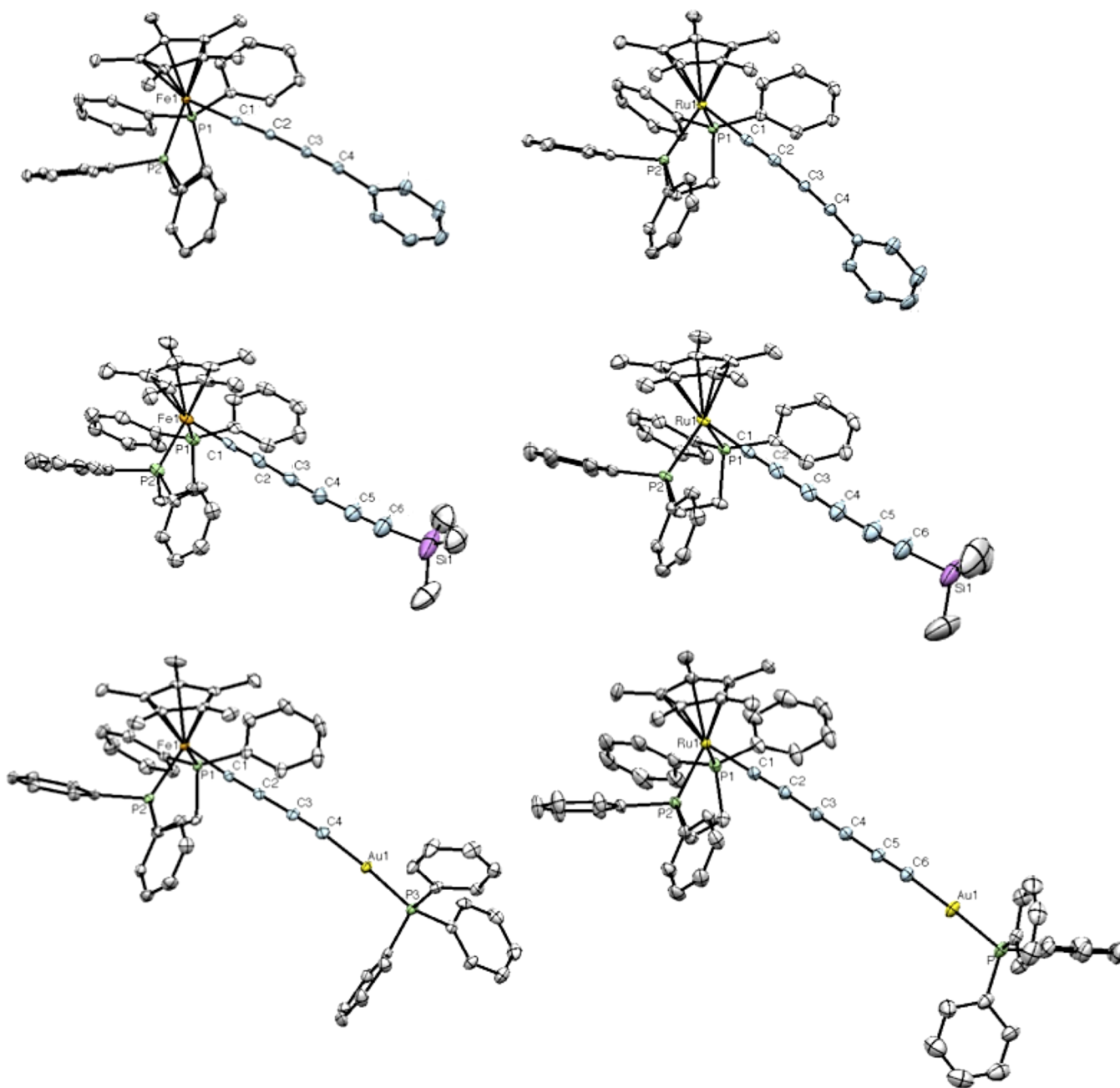


Figure 1. Molecular structures of the isomorphous systems **Fe-2-Ph** (top left) and **Ru-2-Ph** (top right), of **Fe-3-SiMe₃** (middle left) and **Ru-3-SiMe₃** (middle right), and of **Fe-2-Au(PPh₃)** (bottom left) and **Ru-3-Au(PPh₃)** (bottom right), (mol. 1 in each case) showing thermal ellipsoids at the 50% probability level. Hydrogen atoms have been removed for clarity.

compounds of this iron series bearing a hexatrienediyl moiety.^{8,9} Mononuclear iron complexes containing the Fe-(dppf)Cp* fragment and a hexatriynyl ligand have never been synthesized before. The Bruce group has developed a useful methodology for preparing ruthenium complexes with long all-carbon chains with diverse groups on the opposite termini.¹⁰ Following the synthesis of the ruthenium analogue **Ru-3-SiMe₃**,¹⁰ the iron derivative was successfully prepared. The diyne-gold complex **Fe-2-Au(PPh₃)** was treated with an excess of iodo(trimethylsilyl)ethyne in a 1/1 THF/triethylamine mixture in the presence of Pd(PPh₃)₄ and CuI as catalysts (Scheme 3). After workup, the compound **Fe-3-SiMe₃** was obtained as an orange powder in 55% yield.

In addition to the usual spectroscopic characterization, the molecular structure of **Fe-3-SiMe₃** was established by an X-ray crystal structure. The IR spectrum of **Fe-3-SiMe₃** displays only two $\nu(\text{C}\equiv\text{C})$ bands at 2092 and 1952 cm^{-1} . In the ¹³C NMR spectrum, the α -carbon resonates as a triplet at δ 151.07, while the other five carbon atoms of the hexatriynyl ligand appeared as singlets at δ 47.06, 69.29, 77.18, 94.34, and 100.95.

Molecular Structures of Fe-2-Ph, Ru-2-Ph, Fe-2-Au(PPh₃), Fe-3-SiMe₃, Ru-3-SiMe₃, and Ru-3-Au(PPh₃). Plots of single molecules of these complexes are shown in Figure 1; the main bond lengths and angles are summarized in Table S1 (see the Supporting Information), and crystal data and refinement details are summarized in the Experimental Section (Table 10). The crystallographic investigation confirms the

typical pseudo-octahedral geometry of the iron and ruthenium centers.^{4,8,11} All bond distances and bond angles are usual for these types of organo-iron and -ruthenium compounds. The C₄ and C₆ chains are quasi-linear with angles ranging between 174 and 180°. Alternation of short and long carbon–carbon bond lengths confirms the diyanyl or triynyl nature of the chains.

Electrochemical Properties. The redox properties of the polyynyl complexes **Fe-2-Ph**, **Ru-2-Ph**, **Fe-2-Au(PPh₃)**, and **Fe-3-SiMe₃** have been investigated, and the data are compared with those previously obtained for the **Fe-*n*-R** and **Ru-*n*-R** series (*n* = 1–3; R = H, Ph, SiMe₃, Au(PPh₃)).^{4,12,13} The cyclic voltammograms of the polyynyl Fe(II) and Ru(II) complexes were recorded in the ranges –0.4 to +0.5 and –0.4 to +0.9 V vs the standard calomel electrode (SCE), respectively. Interestingly, the degree of chemical reversibility depends not only on the nature of the metal center but also on the carbon chain length and the nature of the terminal R groups. In the iron series, when the carbon chain bears a phenyl ring or a trimethylsilyl group, the heterogeneous electron transfer is fully reversible on the platinum electrode regardless of the number of carbon atoms of the chain. In contrast, for R = H, only partial chemical reversibility is found at a scan rate of 0.100 V/s, and the *i*_{pc}/*i*_{pa} current ratio decreases with the number of carbon–carbon triple bonds in the carbon chain (see Table 1),

Table 1. Electrochemical and IR Data for Fe-*n*-R and Ru-*n*-R Complexes (*n* = 1–3; R = H, Ph, SiMe₃, Au(PPh₃))

compd	<i>E</i> ^o (V/SCE) ^a	<i>i</i> _{pc} / <i>i</i> _{pa}	$\nu_{C\equiv C}$ (cm ⁻¹)	ref
Fe-1-H	-0.12	0.80	1910 ^b	14
Fe-1-Ph	-0.15	1.0	2049 ^b (2053 ^d)	15
Fe-2-Ph	-0.02	1.0	2150, 2007, 1987 ^c	this work
Fe-2-H	0.00	0.48	2099, 1958 ^b	6
Fe-2-SiMe ₃	0.00	1.0	2165, 2090, 1980 ^b	6
Fe-2-Au(PPh ₃)	-0.16	0.61	2069, 1969 ^d	this work
Fe-3-SiMe ₃	0.08	1.0	2092, 1952 ^d	this work
Ru-1-H	0.31	0.8	1930 ^d	3
Ru-1-Ph	0.23	0.8	2071 ^d	13
Ru-2-Ph	0.44	0.02	2153, 2016 ^d	this work
Ru-2-H	0.44	0	2109, 1971 ^b	5
Ru-2-SiMe ₃	0.43	0	2171, 2095, 1990 ^b	5
Ru-2-Au(PPh ₃)	0.15	0	2119, 2072, 1981 ^b	5
Ru-3-SiMe ₃	0.41	0	2110, 1971 ^b	10
Ru-3-Au(PPh ₃)			2121, 2088, 1965 ^b	10

^aConditions: in CH₂Cl₂, 0.1 M [NBu₄]ⁿPF₆, scan rate 0.1 V/s, Pt electrodes, V vs SCE (FeCp₂/[FeCp₂]⁺ = 0.46 V vs SCE used as internal reference for potential measurements).¹⁶ ^bNujol/KBr windows. ^cKBr pellet. ^dCH₂Cl₂/KBr windows.

indicating that the kinetic stability of the Fe(III) complexes on the platinum electrode decreases in the same order. For any carbon chain length, the stability of the Fe(III) complexes decreases with R according to the sequence Ph > SiMe₃ > Au(PPh₃) > H.

Previous work has shown that the kinetic stabilities and the reactivities of the monoalkynyl radicals [*M*(dppe)Cp*]–(C≡C)–H]⁺ (M = Fe, Ru) are very similar. Both radical cations slowly dimerize in solution to produce bis(vinylidene) complexes.^{3,14} While both the iron and ruthenium cations [*M*-1-Ph]⁺ are stable in the solid state and in solution,^{12,15} they have significantly different electronic structures,¹³ which results in the rich reactivity recently reported for [Ru-1-Ph]⁺.¹⁷ Figure

2 nicely illustrates the difference in chemical reversibility for the one-electron oxidations of the iron and ruthenium diyynyls Fe-

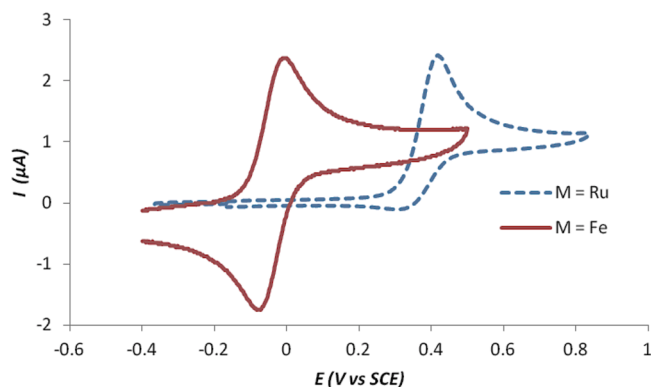


Figure 2. Cyclic voltammograms of **Fe-2-Ph** (solid line, in red) and **Ru-2-Ph** (dotted line, in blue). Experimental conditions are given in Table 1.

2-Ph and **Ru-2-Ph**. In the ruthenium series, the electron transfer is quasi-irreversible on the platinum electrode and replacement of the phenyl group by H, SiMe₃, and Au(PPh₃) makes the electron transfer fully irreversible. For the higher homologues **Ru-3-SiMe₃**, the oxidation is also fully irreversible.

In both series, the redox center senses the electronic effect of the terminal R group. The *E*^o values range from –0.16 to +0.08 V and from +0.15 to +0.44 V in the iron and ruthenium series, respectively. The Au(PPh₃) and phenyl termini are apparently electron-releasing groups to the electroactive center, while the trimethylsilyl and hydrogen substituents show weak electron-withdrawing properties. It is noteworthy that the gold fragment shows unexpected behavior. While its presence renders the complex easier to oxidize, it does not contribute to the stabilization of the resulting radical cation.

In Situ Glass EPR Spectroscopy of [Fe-*n*-R](PF₆) and [Ru-*n*-R](PF₆). The compounds **Fe-*n*-R** and **Ru-*n*-R** were reacted with less than 1 equiv of [FeCp₂](PF₆) in CH₂Cl₂ at –80 °C directly in the quartz EPR tube, and the resulting mixtures were immediately cooled to liquid nitrogen temperature. The X-band EPR spectra of the radical cations generated in situ at 66 K display three well-resolved features corresponding to the components of the *g*-tensors characteristic of d⁵ low-spin Fe(III) and Ru(III) in a pseudo-octahedral environment. The *g*-tensor values extracted from the spectra are collected in Table 2.

Solutions of these radical cations are all stable at low temperature when they are kept as a glass. As the temperature is allowed to increase, the glass melts and rapid decomposition of the organometallic materials takes place, except for the Fe(III) radical cations [{Fe(dppe)Cp*}–(C≡C)–Ph](PF₆) ([**Fe-1-Ph**](PF₆)) and [{Fe(dppe)Cp*}–(C≡C)–SiMe₃](PF₆) ([**Fe-1-SiMe₃**](PF₆)), which are stable in solution at –20 °C. Replacing iron by ruthenium or increasing the number of carbon atoms in the polyynyl ligand decreases the kinetic stability of the radical cations. In the case of R = Ph and *n* = 2, the disappearance of the radical is associated with a decrease in intensity of the EPR signal, suggesting that a radical coupling process occurs. In the other cases, the appearance of several new signals in the spectra indicates that the radicals decompose to give several byproducts, some of them being paramagnetic.

Table 2. Experimental EPR Data^a for Selected $[\{M(\text{dppe})\text{Cp}^*\}-(\text{C}\equiv\text{C})_n-\text{R}](\text{PF}_6)$ Complexes

compd	g_1	g_2 (a_2^f)	g_3 (a_3^f)	Δg	g_{iso}
[Fe-1-Ph] ^{+ b}	2.464	2.033	1.975	0.489	2.157
[Fe-2-Ph] ^{+ b}	2.335	1.937	1.881	0.454	2.051
[Fe-1-SiMe ₃] ^{+ b,c}	2.488	2.030	1.975	0.513	2.164
[Fe-2-SiMe ₃] ^{+ c,d}	2.476	2.032	1.971	0.505	2.160
[Fe-3-SiMe ₃] ^{+ d}	2.475	2.030	1.971	0.504	2.159
[Fe-2-Au(PPh ₃)] ^{+ d,e}	2.401	2.084	1.994	0.407	2.160
[Ru-1-Ph] ^{+ b}	2.227	2.057	1.988	0.239	2.091
[Ru-2-Ph] ^{+ d}	2.418	2.086 (35)	1.998 (55)	0.420	2.167
[Ru-1-SiMe ₃] ^{+ c,d}	2.345	2.069	1.974	0.371	2.129
[Ru-2-SiMe ₃] ^{+ c-e}	2.273	2.048	1.988	0.285	2.103
[Ru-3-SiMe ₃] ^{+ c-e}	2.299	2.040 (41)	1.975 (40)	0.324	2.105
[Ru-2-Au(PPh ₃)] ^{+ c-e}	2.275	2.051	1.986	0.289	2.104
[Ru-3-Au(PPh ₃)] ^{+ c-e}	2.100	2.034 (40)	2.004 (25)	0.096	2.046

^aAt 66 K in CH₂Cl₂ glass; [FeCp₂]⁺PF₆⁻ was used as the oxidizing reagent. ^bThe M(III) radical cation is thermally stable at 20 °C for at least a few minutes in the EPR tube. ^cComplexes prepared using methods cited in Table 1. ^dThe M(III) radical cation is not thermally stable above -20 °C. ^eThe EPR spectrum contains significant amounts of paramagnetic impurities. ^fIn gauss.

For the iron complexes of this series, the g -tensor anisotropies (Δg) are large, ranging from 0.513 to 0.407; they are not very sensitive to the number of carbon atoms in the polyyne ligand and the nature of R. In contrast, for the ruthenium analogues, the Δg parameters range from 0.420 to 0.096, showing that the localization of spin density is strongly dependent both on the number of carbon atoms in the polyyne fragment and on the nature of the terminal substituents. When the Fe and Ru analogues are compared (same chain length and same substituent), the Δg parameters are smaller overall in the ruthenium series. These observations are in line with previous experimental and theoretical results which concluded that the spin density is mainly localized on the metal center in the iron series but largely distributed between the metal and the unsaturated ligand in the case of the ruthenium complexes.¹³

In the ruthenium series, the data should be considered with caution, due to the high instability of the Ru(III) compounds, and we cannot exclude the possibility that the active EPR species observed in the spectra is not the original oxidized species but a radical resulting from its thermal evolution. Assuming that the $[\text{Ru}-n-\text{R}]^{\bullet+}$ radicals were effectively quenched in the glass, the Δg values decrease when the number of carbon atoms increases for R = SiMe₃, Ph, Au(PPh₃), but this correlation is far from being linear. In addition, for a given value of n , the Δg tensors are generally smaller for R = SiMe₃, Au(PPh₃), which have spherical symmetry, than for the planar phenyl substituent. Serious doubts arise concerning the almost identical EPR results obtained for $[\text{Ru}-2-\text{SiMe}_3]^+$ and $[\text{Ru}-2-\text{Au}(\text{PPh}_3)]^+$, suggesting that the same decomposition product was measured.

■ COMPUTATIONAL RESULTS AND DISCUSSION

DFT calculations (BP86/TZP) were performed on the series of mononuclear complexes $[\text{Fe}-n-\text{R}]^{0/+}$ and $[\text{Ru}-n-\text{R}]^{0/+}$, for $n = 1-3$ and R = H, Ph and for $n = 2$ and R = SiMe₃, Au(PPh₃), in

order to understand how the nature of the metal, the length of the carbon chain, and the nature of the R substituent affect their electronic properties. All systems considered were fully optimized without symmetry constraints (see Computational Details).

Effect of the Length of the Carbon Chain. The effect of lengthening the carbon chain on the electronic and physical properties was investigated going from alkynyl to triynyl chains in the iron and ruthenium series. This study, which also includes the effect of oxidation, is limited to R = H, Ph. Pertinent computed metric data are reported in Tables 3 and 4 for iron and ruthenium complexes, respectively. They are compared to the experimental data where available. The optimized geometries of Fe- n -R ($n = 1-3$) compare rather well with those obtained by X-ray diffraction. The largest bond distance deviations between calculated and experimental results are found for Fe-Cp*(centroid) and Fe-P(dppe) distances, which are computationally overestimated by 0.06 and 0.04 Å, respectively. The rest of the bond lengths are reproduced well, the C≡C triple bonds being computed as only 0.02 Å too long. Such deviations between theory and experiment are typical for this kind of organometallic system at this level of theory.¹⁷⁻¹⁹

The lengthening of the carbon chain from Fe-1-H to Fe-3-H hardly changes the metal-ligand (Cp*, dppe) distances. In contrast, the metal-carbon backbone is more affected. The Fe-C₁ bond length shortens from 1.905 to 1.858 Å, while the C≡C triple bonds slightly lengthen (+0.02 Å for C₁≡C₂) and the C-C single bonds shorten (-0.02 Å for C₂-C₃) upon chain lengthening. For the {Cp(PH₃)₂Ru}-(C≡C)_n-Ph ($n = 1-6$) analogues, the same trend was observed.²⁰ The geometrical analyses of Fe- n -Ph and Ru- n -R ($n = 1-3$) compounds lead to exactly the same conclusions, in agreement with the experimental trends.

Electronic structures of these polyyne complexes were investigated. Overall, they are similar (see Figure S1 in the Supporting Information). Using the Fe- n -H series as an example, we see that the highest occupied molecular orbital (HOMO) and HOMO-1 are $d\pi/\pi$ type in character, antibonding between the Fe and C₁ atoms and the carbon atoms of the chain involved in a single bond, and bonding between the carbon atoms of the triple bonds (Figure 3). Their spatial extensions are in two distinct perpendicular planes, the HOMO lying in the π network orthogonal to the polyyne ligand, whereas the HOMO-1 sits in the parallel plane. The lowest unoccupied molecular orbital (LUMO) is metal-ligand (Cp*, dppe) antibonding in character in all cases, and the LUMO+1 is π^* dppe centered.²²

Although the energies and nodal properties of the MOs are somewhat modified, the lengthening of the carbon chain hardly affects the HOMO-LUMO energy gap within the series, which is roughly 1.7 eV, because of an overall stabilization of the energy levels. Indeed, replacement of the (C≡C)-H fragment by a (C≡C)₃-H fragment stabilizes the first HOMOs by only 0.30 eV. This is associated with a diminishing of the iron contribution to the first HOMOs, from 63% for the Fe-1-H complex to 44% for the Fe-3-H complex, and with a consequent increase of the carbon chain character from 20% to 42% (see Table S2 in the Supporting Information). The shortening of the metal-carbon distance upon lengthening of the chain is thus due to a smaller antibonding π interaction and also to a reinforced σ bond (deeper MOs). The first LUMOs are also stabilized by 0.33 eV on going from Fe-1-H to Fe-3-H, mainly because of the electrostatic contributions. This analysis

Table 3. Pertinent Optimized Bond Lengths (Å), $\nu_{C\equiv C}$ Bond Stretching (cm^{-1}), and Ionization Potentials (IP, eV) for $[\text{Fe}-n\text{H}]^{0/+}$ and $[\text{Fe}-n\text{Ph}]^{0/+}$ ($n = 1-3$), in Comparison with the Corresponding Experimental Data Given in Parentheses Where Available

compd	charge	Fe-P	Fe-Cp*	Fe-C ₁	C ₁ ≡C ₂	C ₂ -C ₃	C ₃ ≡C ₄	C ₄ -C ₅	C ₅ ≡C ₆	C _n -R	$\nu_{C\equiv C}$	IP ^d /IP ^e _{solv}
Fe-1-H	0	2.214/2.205 (2.175/2.177)	1.799 (1.741)	1.905 (1.876)	1.234 (1.210)					1.070	1913 (1910) ^a	5.35/4.44
	1+	2.303/2.290	1.830	1.885	1.233					1.073	1907	
Fe-2-H	0	2.221/2.213	1.800	1.875	1.247	1.357	1.228			1.067	2017, 2273	5.42/4.60
	1+	2.297/2.286	1.829	1.847	1.251	1.349	1.225			1.069	1814, 1960	
Fe-3-H	0	2.225/2.218	1.803	1.858	1.252	1.341	1.242	1.348	1.227	1.067	1846, 1983, 2039	5.46/4.71
	1+	2.280/2.294	1.829	1.828	1.258	1.330	1.243	1.343	1.225	1.069	1780, 1946, 2001	
Fe-1-Ph	0	2.204/2.207 (2.174/2.185)	1.800 (1.740)	1.897 (1.894)	1.240 (1.210)					1.423 (1.430)	1945 (2053) ^b	5.30/4.44
	1+	2.263/2.279	1.835	1.863	1.243					1.418	2008	
Fe-2-Ph	0	2.224/2.214 (2.181/2.196)	1.799 (1.746)	1.870 (1.873)	1.249 (1.230)	1.351 (1.372)	1.234 (1.211)			1.416 (1.434)	1981, 2144 (1987, 2007, 2150) ^c	5.26/4.49
	1+	2.282/2.268	1.825	1.829	1.255	1.339	1.236			1.411	1832, 2001	
Fe-3-Ph	0	2.229/2.220	1.801	1.857	1.253	1.338	1.244	1.342	1.234	1.415	1868, 2014, 2049	5.31/4.63
	1+	2.282/2.276	1.825	1.822	1.262	1.326	1.248	1.332	1.237	1.408	1787, 1953, 2027	

^aSee ref 21. ^bSee ref 4. ^cThis work. Cp* = centroid. ^dComputed adiabatic ionization potential. ^eComputed adiabatic ionization potential with solvent effects.

Table 4. Pertinent Optimized Bond Lengths (Å) and Ionization Potentials (IP, eV) for $[\text{Ru}-n\text{H}]^{0/+}$ and $[\text{Ru}-n\text{Ph}]^{0/+}$ ($n = 1-3$), in Comparison with the Corresponding Experimental Data Given in Parentheses Where Available

compd	charge	Ru-P	Ru-Cp*	Ru-C ₁	C ₁ ≡C ₂	C ₂ -C ₃	C ₃ ≡C ₄	C ₄ -C ₅	C ₅ ≡C ₆	C _n -R	IP ^d /IP ^e _{solv}
Ru-1-H	0	2.303/2.315 (2.259/2.265)	2.009 (1.883)	2.038 (2.015)	1.233 (1.202) ^a					1.068	5.67/4.80
	1+	2.361/2.378	2.026	1.994	1.239					1.069	
Ru-2-H	0	2.313/2.325 (2.256/2.279)	2.005 (1.895)	2.009 (2.015)	1.245 (1.186)	1.356 (1.387)	1.227 (1.193) ^b			1.066	5.67/4.90
	1+	2.364/2.377	2.027	1.957	1.257	1.344	1.228			1.068	
Ru-3-H	0	2.318/2.330	2.008	1.994	1.251	1.340	1.241	1.349	1.227	1.066	5.67/4.96
	1+	2.364/2.377	2.024	1.941	1.264	1.324	1.246	1.341	1.226	1.068	
Ru-1-Ph	0	2.308/2.308 (2.256/2.262)	2.009 (1.884)	2.030 (2.011)	1.240 (1.215)					1.424 (1.431) ^c	5.54/4.73
	1+	2.353/2.365	2.025	1.980	1.249					1.413	
Ru-2-Ph	0	2.329/2.317 (2.261/2.277)	1.996 (1.896)	2.008 (1.997)	1.247 (1.202)	1.350 (1.377)	1.235 (1.211)			1.417 (1.429) ^f	5.47/4.72
	1+	2.372/2.359	2.021	1.953	1.262	1.334	1.240			1.409	
Ru-3-Ph	0	2.332/2.319	2.004	1.996	1.252	1.339	1.244	1.343	1.234	1.415	5.56/5.12
	1+	2.355/2.380	2.020	1.940	1.267	1.321	1.251	1.331	1.238	1.411	

^aSee ref 3. ^bSee ref 5. ^cComputed adiabatic ionization potential. ^dComputed adiabatic ionization potential with solvent effects. ^eSee ref 13. ^fThis work. Cp* = centroid.

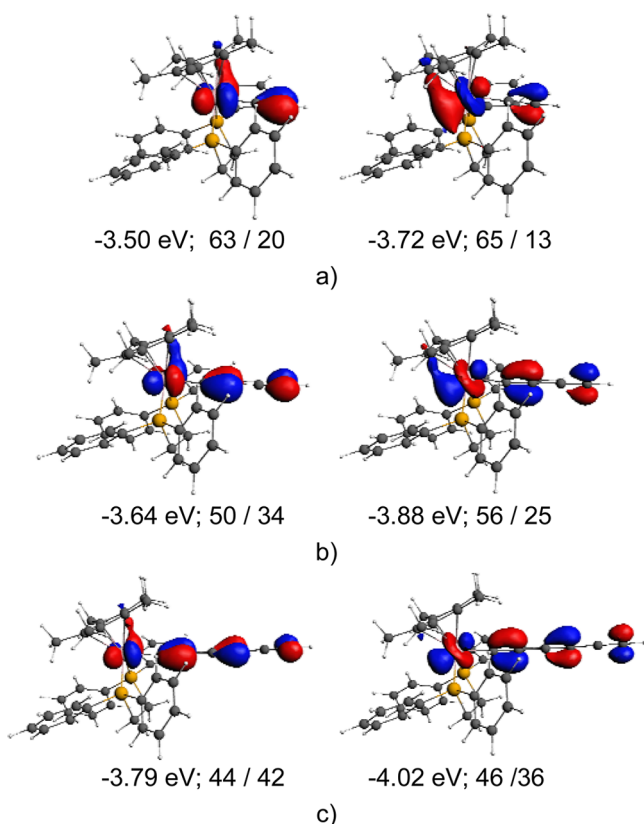


Figure 3. Contour plots, energies, and Fe/C_n percentages of the HOMO (left) and HOMO-1 (right) of (a) **Fe-1-H**, (b) **Fe-2-H**, and (c) **Fe-3-H**. Contour values are ± 0.045 (e/bohr³)^{1/2}.

of the changes in the electronic structure upon carbon chain lengthening is also relevant to the phenyl-substituted series **Fe-*n*-Ph** ($n = 1-3$), even though the first HOMOs can possess additionally also a subsequent phenyl character. The analysis done above is qualitatively the same for the closely related **Ru-*n*-R** ($n = 1-3$; R = H, Ph) series. However, the two first HOMOs of the ruthenium compounds are less metal-centered than the corresponding ones in the iron series, with a Ru percentage ranging from 25 to 49% (44–63% for Fe).

To quantify the differences between ruthenium- and iron-containing systems, an analysis of the different terms of the metal–carbon chain bond energy was performed (see Table 5).²³ This approach decomposes the bond dissociation energy (ΔE_{BDE}) between the metal fragment and the carbon chain as a sum of orbital interactions (ΔE_{orb}), electrostatic contributions (ΔE_{el}), and Pauli repulsion interactions (ΔE_{Pauli}). Interestingly, the orbital interactions are largely similar for both metals, probably with compensation between σ bonding and d/π

Table 5. Heterolytic Bond Dissociation Energies (BDEs) of the M–C₁ Bond for **Fe-1-Ph** and **Ru-1-Ph** (in eV)

compd	Fe-1-Ph	Ru-1-Ph
ΔE_{Pauli}	+9.27	+9.92
ΔE_{orb}	−4.67	−4.63
ΔE_{el}	−10.86	−11.41
ΔE_{BDE}^a	−6.26	−6.12
ΔE_{BDE}^b	−6.18	−6.05

^aWithout basis set superposition error (BSSE) correction. ^bWith BSSE correction.

bonding. The geometry relaxations of the fragments do not modify these observations (see Tables S7–S10 in the Supporting Information). The main difference in M–C interaction arises from the electrostatic attraction and the Pauli repulsion. Overall, the latter is more important in **Ru-1-Ph** and explains the weaker Ru–carbon bond. Electrostatic and Pauli interactions cannot be deduced from orbital properties. This prevents drawing any conclusions about the difference between Fe- and Ru-containing systems from orbital analysis alone.

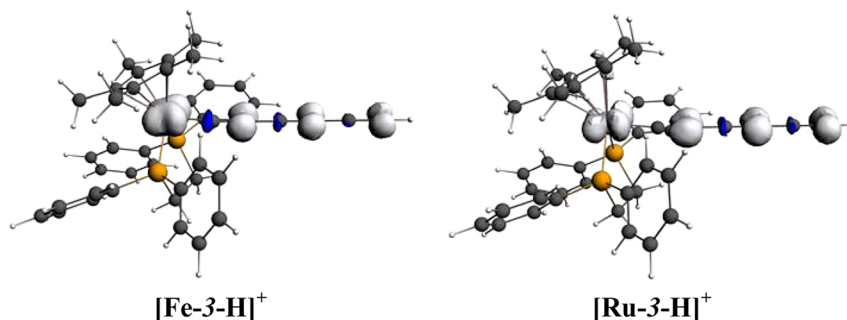
The oxidized open-shell systems $[\text{M-}n\text{-R}]^+$ were also considered. As expected, the metal–ligand (Cp*, dppe) bond lengths are elongated upon oxidation, but to a lesser extent with increasing chain length. The computed elongations for the Fe–Cp* bond lengths are 0.03 and 0.03 Å for $[\text{Fe-1-H}]^+$ and $[\text{Fe-3-H}]^+$, respectively, and the computed lengthening for the Fe–P(dppe) distances are 0.09 and 0.06 Å for $[\text{Fe-1-H}]^+$ and $[\text{Fe-3-H}]^+$, respectively. The Fe–C and C–C distances are also affected upon oxidation. The Fe–C₁ bond is diminished by roughly 0.03 Å, while the C–C single bonds and C≡C triple bonds alternately shorten and lengthen to a lesser extent. These changes are consistent with the nodal properties of the HOMOs (see above), considering that the oxidation process corresponds formally to removal of an electron from one of the two highest occupied MOs. This illustrates the fact that the oxidation takes place not only on the metal atom but also on the carbon chain. This is particularly the case for the ruthenium series, for which the HOMOs are more localized on the carbon chain. The ruthenium–ligand bond lengths are thus less affected upon oxidation than in the iron series. Similar trends were previously found for related arylvinyl ruthenium compounds, where the first HOMOs are fully delocalized along the ruthenium–arylvinyl unit.²⁴

Atomic spin densities were computed by means of the Mulliken population analysis technique for monocationic species in order to describe the delocalization of the unpaired electron. The results are summarized in Scheme 4 for $[\text{Fe-}n\text{-H}]^+$ and $[\text{Ru-}n\text{-H}]^+$ complexes, and the spatial distributions of the computed spin density for $[\text{Fe-3-H}]^+$ and $[\text{Ru-3-H}]^+$ are shown in Figure 4. The largest part of the positive spin density is located on the metal center for both series of complexes. The rest is distributed over the even-numbered carbon atoms. The atomic spin density on the metal decreases with lengthening of the carbon chain, from 0.96 electron (e) to 0.74 e, and from 0.53 to 0.36 e for $[\text{Fe-}n\text{-H}]^+$ and for $[\text{Ru-}n\text{-H}]^+$ respectively, on going from $n = 1$ to 3. Consequently, the spin density is more localized on the organic chain but divided on more atoms.

The adiabatic ionization potentials (IPs) were computed for several carbon chain lengths and are given in Tables 3 and 4 for iron and ruthenium complexes, respectively. For the **Fe-*n*-H** series, the oxidation is found to become more difficult with increasing n (5.35, 5.42, and 5.46 eV for $n = 1-3$, respectively), in agreement with the experimental redox potentials (E°). For **Ru-*n*-H**, the calculated IPs are unchanged for $n = 1$ to $n = 3$ (5.67 eV), whereas a noticeable increase is measured in the oxidation potentials (0.23 and 0.44 V for $n = 1, 2$, respectively). In the type of systems studied here, solvation energies of neutral and oxidized compounds are different, due to the fact that the unprotected carbon chain is affected upon oxidation. They do not compensate and thus cannot be neglected. The IP_{solv} values, including solvation corrections, were thus calculated (see Tables 3 and 4 and Computational Details). For **Fe-*n*-H**, **Ru-*n*-H**, and **Fe-*n*-Ph**, oxidation in a solvent is

Scheme 4. Calculated Atomic Spin Densities for $[\text{Fe}-n\text{-H}]^+$ and $[\text{Ru}-n\text{-H}]^+$ Complexes

0.96 -0.10 0.25 [Fe]—C ₁ ≡C ₂ —H	0.53 -0.08 0.32 [Ru]—C ₁ ≡C ₂ —H
0.83 -0.10 0.23 -0.07 0.20 [Fe]—C ₁ ≡C ₂ —C ₃ ≡C ₄ —H	0.43 -0.06 0.27 -0.08 0.25 [Ru]—C ₁ ≡C ₂ —C ₃ ≡C ₄ —H
0.74 -0.09 0.21 -0.08 0.19 -0.06 0.17 [Fe]—C ₁ ≡C ₂ —C ₃ ≡C ₄ —C ₅ ≡C ₆ —H	0.36 -0.05 0.24 -0.08 0.23 -0.07 0.21 [Ru]—C ₁ ≡C ₂ —C ₃ ≡C ₄ —C ₅ ≡C ₆ —H

Figure 4. Spatial distributions of computed spin density of $[\text{Fe}-3\text{-H}]^+$ (left) and $[\text{Ru}-3\text{-H}]^+$ (right). Isocontour value: ± 0.005 e/bohr³.Table 6. Pertinent Optimized Bond Lengths (Å) and Ionization Potentials (IP, eV) for $[\text{Fe}-2\text{-R}]^{0/+}$ (R = H, Ph, SiMe₃, Au(PPh₃)), in Comparison with the Corresponding Experimental Data Given in Parentheses Where Available

compd	charge	Fe–P	Fe–Cp*	Fe–C ₁	C ₁ ≡C ₂	C ₂ –C ₃	C ₃ ≡C ₄	C ₄ –R	IP
Fe-2-H	0	2.221/2.213	1.800	1.875	1.247	1.357	1.228	1.067	5.42
	1+	2.297/2.286	1.829	1.847	1.251	1.349	1.225	1.069	
Fe-2-Ph	0	2.224/2.214 (2.181/2.196)	1.799 (1.746)	1.870 (1.873)	1.249 (1.230)	1.351 (1.372)	1.234 (1.211)	1.416 (1.434) ^a	5.26
	1+	2.282/2.268	1.825	1.829	1.255	1.339	1.236	1.411	
Fe-2-SiMe ₃	0	2.215/2.218 (2.180/2.188)	1.801 (1.742)	1.868 (1.874)	1.248 (1.227)	1.351 (1.374)	1.241 (1.220)	1.823 (1.822) _{b,c}	5.35
	1+	2.280/2.297	1.831	1.842	1.253	1.341	1.241	1.856	
Fe-2-Au(PPh ₃) ^d	0	2.206/2.212 (2.181/2.180)	1.797 (1.741)	1.882 (1.875)	1.249 (1.237)	1.356 (1.371)	1.243 (1.217)	1.980 (1.986) ^a	4.80
	1+	2.262/2.275	1.824	1.837	1.257	1.343	1.247	1.990	

^aThis work. ^bSee ref 5. ^cSee ref 6. ^dRelativistic effects included; see Computational Details. Cp* = centroid.Table 7. Pertinent Optimized Bond Lengths (Å) and Ionization Potentials (IP, eV) for $[\text{Ru}-2\text{-R}]^{0/+}$ (R = H, Ph, SiMe₃, Au(PPh₃)), in Comparison with the Corresponding Experimental Data Given in Parentheses Where Available

compd	charge	Ru–P	Ru–Cp*	Ru–C ₁	C ₁ ≡C ₂	C ₂ –C ₃	C ₃ ≡C ₄	C ₄ –R	IP
Ru-2-H	0	2.313/2.325 (2.256/2.279)	2.005 (1.883)	2.009 (2.015)	1.245 (1.186)	1.356 (1.387)	1.227 (1.193) ^a	1.066	5.67
	1+	2.364/2.377	2.027	1.957	1.257	1.344	1.228	1.068	
Ru-2-Ph	0	2.317/2.329 (2.261/2.277)	1.996 (1.896)	2.008 (1.997)	1.247 (1.202)	1.350 (1.377)	1.235 (1.211)	1.417 (1.429) ^b	5.47
	1+	2.359/2.372	2.021	1.953	1.262	1.334	1.240	1.409	
Ru-2-SiMe ₃	0	2.321/2.326 (2.261/2.278)	2.007 (1.903)	2.004 (1.983)	1.248 (1.231)	1.353 (1.371)	1.241 (1.222)	1.818 (1.822) ^a	5.58
	1+	2.361/2.374	2.024	1.951	1.261	1.339	1.244	1.849	
Ru-2-Au(PPh ₃) ^c	0	2.283/2.290 (2.262/2.278)	1.949 (1.897)	1.992 (1.992)	1.248 (1.221)	1.357 (1.378)	1.243 (1.205)	1.976 (1.992) ^a	5.02
	1+	2.336/2.350	1.999	1.938	1.266	1.339	1.248	1.985	

^aSee ref 5. ^bThis work. ^cRelativistic effects included; see Computational Details. Cp* = centroid.

calculated to become more difficult with increasing n . This agrees with the available experimental data. For **Ru- n -Ph**, similar IP_{solv} values are calculated for $n = 1, 2$. This can be explained by the geometry fluctuation detailed below.

Effects of the R Substituents. To analyze the effects of end groups R on the electronic properties, DFT calculations were carried out on two representative examples: namely, $[\text{Fe}-$

$2\text{-R}]^{0/+}$ and $[\text{Ru}-2\text{-R}]^{0/+}$ (R = H, Ph, SiMe₃, Au(PPh₃)). The main optimized bond lengths obtained for the different R groups (R = H, Ph, SiMe₃, Au(PPh₃)) in the neutral and monocationic species are reported in Tables 6 and 7 for $[\text{Fe}-2\text{-R}]^{0/+}$ and $[\text{Ru}-2\text{-R}]^{0/+}$, respectively, and are compared to experimental bond lengths where available. The analysis of the optimized structures reveals that the computed bond lengths in

the chain are not significantly affected by the substitution ligand. In the ruthenium series, the main differences between experimental and calculated structures are found for Ru–P(dppe) and Ru–Cp* bond lengths which are computed to be longer by 0.05 and 0.10 Å, respectively. These discrepancies in the M–P(dppe) and M–Cp* centroid lengths are the same as those found previously, except in the case of R = Au(PPh₃), for which the agreement is much better, with computed elongations of 0.02 and 0.04 Å for Ru–P(dppe) and Ru–Cp*, respectively.¹⁹

The calculated Ru–C₁ separation deviates by up to 0.02 Å from the experimental X-ray results, whereas the maximum deviation in the C–C distances within the chain is 0.04 Å. Nevertheless, in all cases, the total lengths of the metal–carbon chains (Ru–C_n) are in good agreement with the experimental data, with a discrepancy of less than 0.06 Å for the sum of the four bond distances for the triynyl complexes. In fact, the homogeneous delocalization of the electron density along the metal–carbon chain often leads to imprecise experimental positioning of the atoms.

Energies and isosurfaces of the HOMOs and LUMOs for Ru-2-R complexes are shown in Figure 5. All HOMO–LUMO energy gaps are computed to be roughly 1.9 eV, except for the

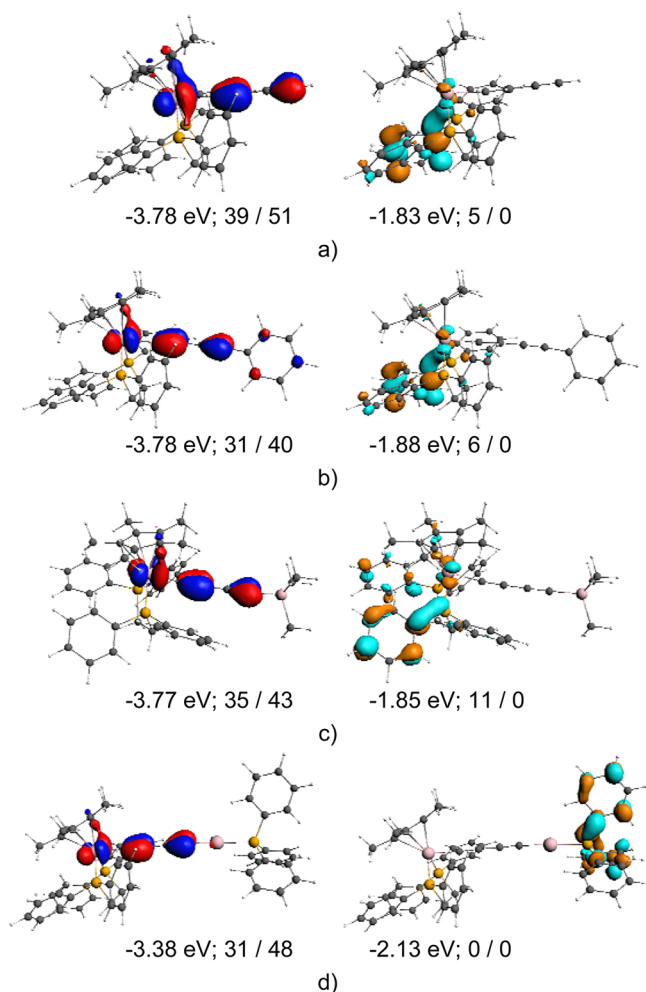


Figure 5. Contour plots, energies, and Ru/C₄ percentages of the HOMO (left) and of the LUMO (right) for (a) Ru-2-H, (b) Ru-2-Ph, (c) Ru-2-SiMe₃, and (d) Ru-2-Au(PPh₃). Contour values: ± 0.045 (e/bohr³)^{1/2}.

Au(PPh₃)-containing complex, for which it is calculated to be 1.2 eV. In the latter case, the two first LUMOs are mainly Au(PPh₃)-centered, in contrast with the other complexes of the series, where the first LUMOs are Ru–ligand (Cp*, dppe) antibonding molecular orbitals or π^* on the phenyl groups of the dppe. For R = Au(PPh₃), the antibonding MOs centered on the metal atom are the LUMO+2 and LUMO+5, lying roughly 1.7 eV above the HOMO found in the other complexes (see Figure S2 in the Supporting Information). In all cases, as found for R = H, Ph, the first HOMOs are fully delocalized on the metal–carbon chain and have an important antibonding character between the metal center and atom C₁. For the Au(PPh₃)-containing complex, the carbon chain character is roughly 50%, in comparison to 40% for the other complexes, whereas the metal character is unchanged.

The IPs were computed for the different end groups and compared to the corresponding experimental redox potentials. The computed IPs values slightly diminish from 5.7 to 5.6 and 5.5 eV when H is replaced by SiMe₃ and phenyl groups, respectively, suggesting that these compounds have similar oxidative properties. Experimentally, this trend is confirmed by the measured redox potentials, which show similar values (0.44 and 0.43 V for R = Ph, SiMe₃, respectively). The computed HOMO energies stay approximately constant for these substituents and confirm this trend theoretically. The easiest complex to oxidize is found both theoretically (IP = 5.0 eV) and experimentally ($E^\circ = 0.15$ V) for R = Au(PPh₃).⁵

The spin density distributions computed for [Ru-2-R]⁺ cations are given in Scheme 5. The largest positive atomic spin density is found associated with the metal atom, but as expected, our calculations also reveal that the unpaired electron is partly delocalized on the even-numbered carbon atoms of the chain. The atomic spin density on the C₄ atom is strongly influenced by the nature of the substituent. The smallest value is found for the phenyl substituent (0.21 e), since a part of the unpaired electron density is also delocalized on the phenyl end group (following the HOMOs spatial properties, see above). The atomic spin densities computed on the C₄ atom for the H, SiMe₃, and Au(PPh₃) substituents are 0.25, 0.28, and 0.30 e, respectively. This increase has to be correlated with the donor character of the substituent (H < SiMe₃ < Au(PPh₃)). The same trend is observed with the iron complexes but with a more important localization of the unpaired electron on the metal atom and less on the carbon chain, in comparison with the ruthenium analogues, as expected. Indeed, the oxidation of the [Ru-2-R]⁺ compounds is partly or fully irreversible, whereas [Fe-2-R]⁺ are more stable.

The atomic spin density on the carbon chain can also be correlated to the instability within the [M-2-R]⁺ series. A non-negligible spin density is found for the C₂ atom, but it is less than that for the analogous [M-1-R]⁺. The latter dimerizes for R = H, for which the C₂ atomic spin density is the highest. For $n = 2$, spin density is more concentrated on the C₄ atoms with the largest value calculated for R = SiMe₃, Au(PPh₃) (see Scheme 5). This is particularly the case for [Ru-2-R]⁺, for which 0.28 and 0.30 e are calculated, respectively. This favors radical–radical reactions, with traces of O₂ for example.²⁵ On this basis, the stability would be Ph > H > SiMe₃ > Au(PPh₃), with ruthenium systems less stable in any case. Nevertheless, the bulkiness of SiMe₃ and Au(PPh₃) can slow down the process and would explain the Ph > SiMe₃ > Au(PPh₃) > H found experimentally by electrochemical studies.

Scheme 5. Calculated Atomic Spin Densities for [Fe-2-R]⁺ and [Ru-2-R]⁺

0.83 -0.10 0.23 -0.07 0.20 [Fe]—C ₁ ≡C ₂ —C ₃ ≡C ₄ —H	0.43 -0.06 0.27 -0.08 0.25 [Ru]—C ₁ ≡C ₂ —C ₃ ≡C ₄ —H
0.70 -0.06 0.20 -0.05 0.17 [Fe]—C ₁ ≡C ₂ —C ₃ ≡C ₄ —Ph	0.36 -0.01 0.22 -0.04 0.21 [Ru]—C ₁ ≡C ₂ —C ₃ ≡C ₄ —Ph
0.79 -0.09 0.22 -0.07 0.22 [Fe]—C ₁ ≡C ₂ —C ₃ ≡C ₄ —SiMe ₃	0.40 -0.04 0.26 -0.08 0.28 [Ru]—C ₁ ≡C ₂ —C ₃ ≡C ₄ —SiMe ₃
0.70 -0.05 0.21 -0.04 0.24 [Fe]—C ₁ ≡C ₂ —C ₃ ≡C ₄ —Au(PPh ₃)	0.36 -0.01 0.27 -0.06 0.30 [Ru]—C ₁ ≡C ₂ —C ₃ ≡C ₄ —Au(PPh ₃)

Table 8. g-Tensor Components and Anisotropies for the [Fe-*n*-R]⁺ and [Ru-*n*-R]⁺ Complexes, with Experimental Values Given in Parentheses Where Available

compd	g ₁	g ₂	g ₃	Δg
[Fe-1-H] ⁺	2.601	2.001	1.900	0.701
[Fe-2-H] ⁺	2.480	2.023	1.930	0.550
[Fe-3-H] ⁺	2.402	2.034	1.948	0.454
[Fe-1-Ph] ⁺	2.499 (2.464)	1.989 (2.033)	1.917 (1.975)	0.582 (0.489)
[Fe-2-Ph] ⁺	2.225 (2.335)	2.037 (1.937)	1.984 (1.881)	0.241 (0.454)
[Fe-3-Ph] ⁺	2.263	2.032	1.977	0.286
[Fe-2-SiMe ₃] ⁺	2.386 (2.476)	2.039 (2.032)	1.950 (1.971)	0.436 (0.505)
[Fe-2-Au(PPh ₃)] ⁺	2.556 (2.401)	2.007 (2.084)	1.898 (1.994)	0.658 (0.407)
[Ru-1-H] ⁺	2.331	2.046	1.946	0.385
[Ru-2-H] ⁺	2.321	2.039	1.949	0.372
[Ru-3-H] ⁺	2.319	2.032	1.954	0.365
[Ru-1-Ph] ⁺	2.283 (2.227)	2.033 (2.057)	1.956 (1.988)	0.327 (0.239)
[Ru-2-Ph] ⁺	2.190 (2.418)	2.049 (2.086)	1.982 (1.998)	0.208 (0.420)
[Ru-3-Ph] ⁺	2.542	1.929	1.860	0.682
[Ru-2-SiMe ₃] ⁺	2.305 (2.273)	2.037 (2.048)	1.952 (1.988)	0.353 (0.285)
[Ru-2-Au(PPh ₃)] ⁺	2.521 (2.275)	1.986 (2.051)	1.899 (1.986)	0.622 (0.289)

EPR Properties. EPR properties of the optimized [Fe-*n*-R]⁺ and [Ru-*n*-R]⁺ complexes were computed (mPBE/TZP). The resulting g-tensor components are given in Table 8. The agreement between the computed and experimental anisotropies Δg is moderately satisfactory. The largest deviation is found for [Ru-2-Au(PPh₃)]⁺, but its low stability suggests that decomposition products are present (see below).

Looking at the computed g-tensor components of the [Fe-*n*-R]⁺ and [Ru-*n*-R]⁺ complexes, some general trends appear. First, the influence of the R group on the main g-tensor components is important and is clearly evidenced by computed Δg anisotropies computed to follow the order H > SiMe₃ ≫ Ph. The presence of a conjugated R group strongly diminishes Δg. Second, the lengthening of the carbon chain in some cases affects the g-tensor components; the computed Δg values overall diminish as the carbon chain becomes longer, but for R = Ph and [Ru-*n*-H]⁺ this is not the case. Third, the computed anisotropies Δg in the iron series are always much larger than those in the ruthenium series, except for R = Ph. These results are roughly understood if one considers, as currently accepted in the literature, that EPR parameters of organometallic compounds are related to the metal spin density distribution.²⁶ As mentioned previously, the computed atomic spin density on the metal center (i) decreases when the hydrogen substituent is replaced by SiMe₃ and by phenyl groups, (ii) decreases as the carbon chain lengthens, and (iii) is always computed to be much larger in the iron series than in ruthenium. In contrast to what is commonly admitted, the calculated Δg values have a different evolution that the calculated atomic spin density on

the metal atom. For example, in the [Ru-*n*-H]⁺ series, the ruthenium spin density goes from 0.53 to 0.36 e for *n* = 1–3 (see Scheme 4), while Δg is calculated to be almost constant (0.38 to 0.36). The same is found for the phenyl-substituted series. A more detailed study is needed to understand this apparent discrepancy.

For R = Au(PPh₃), the computed Δg values are the largest ones, but they are probably overestimated. Indeed, for high atomic number atom containing systems, spin–orbit coupling is known to contribute importantly.²⁷ The ESR module in quantum chemistry code we use does not allow including full spin–orbit coupling but only first-order perturbation corrections (see Computational Details). Nevertheless, one would expect a noticeable change between systems substituted by SiMe₃ and by Au(PPh₃), as measured experimentally for M = Fe. For M = Ru, the g-tensor components and the anisotropies are measured to be almost identical (Δg = 0.29 for both; cf. Table 8). In this case, it is highly probable that some decomposition may have occurred in both cases, as mentioned in the Experimental Section, leading to the measurement of the same decomposition product, as already observed for analogous systems.^{13,25} C₄–R bond breaking can be proposed. Homolytic C₄–R bond dissociation energies (Tables S7–S10 in the Supporting Information) have been calculated to evaluate this possibility. They are effectively much weaker for SiMe₃ and Au(PPh₃) than for H and Ph substituents (4.65–4.88 vs 5.31–5.66 eV), but these bonds are stronger for ruthenium compounds than for the more stable iron systems. The instabilities of [Ru-2-SiMe₃]⁺ and [Ru-2-Au(PPh₃)]⁺ are thus

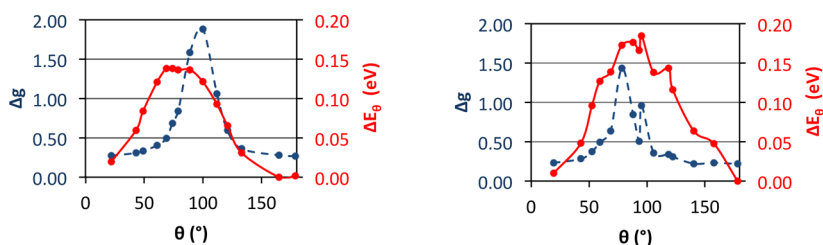


Figure 6. Calculated variation of the anisotropy Δg (in blue, dotted line) and the relative energy ΔE_{θ} (in red, solid line) as a function of the rotation angle θ of the phenyl end group for $[\text{Fe-I-Ph}]^+$ (left) and $[\text{Ru-I-Ph}]^+$ (right).

not due to cleavage of the $\text{C}_4\text{-Si}$ or $\text{C}_4\text{-Au}$ bonds but, as detailed in the previous section, can be attributed to the large atomic spin density on the C_4 atom favoring radical instability.

For $\text{R} = \text{Ph}$, the computed anisotropies do not vary linearly as a function of the metallic spin density, and no clear tendency can be established. In fact, calculations were performed on the most stable optimized structures and do not take into account possible geometrical changes which can occur in solution: i.e., rotation of the phenyl end group ($\theta = \text{Cp}^* \text{ centroid-M-C}_{\text{ipso}}\text{-C}_{\text{ortho}}$).²⁸ It has already been shown, particularly by Paul and co-workers on substituted arylacetylide complexes, that the geometries of the molecules strongly influence the \mathbf{g} -tensor values.^{29,30} They showed that the phenyl orientation plays an important role in the EPR values. In order to evaluate the effect of rotation of the phenyl end groups, 14 different geometrical arrangements of $[\text{Fe-I-Ph}]^+$ with dihedral angles θ ranging from 22° to 179° were investigated (see Computational Details). The EPR properties were computed in each case and are reported in Table S11 (Supporting Information) and plotted in Figure 6. A sizable change in the computed anisotropies is found upon rotation of the phenyl ring. Indeed, the computed anisotropies Δg evolve in a Gaussian way with θ going from 22 to 179° (see left of Figure 6), with a minimum value of 0.27 corresponding to the rotamers $\theta = 22^\circ$ and $\theta = 179^\circ$ (labeled $[\text{Fe-I-Ph-}\perp]^+$),³¹ and a maximum value of 1.88 found at $\theta = 100^\circ$. These results can be correlated approximately with changes in the positive atomic spin densities distribution along the arylalkynyl ligand (Table S11). For the most stable system, $[\text{Fe-I-Ph}]^+$ ($\theta = 165^\circ$), the spin density is spread all along the carbon chain and the phenyl group, whereas for the $\theta = 89^\circ$ rotamer (labeled $[\text{Fe-I-Ph-}\parallel]^+$), it is concentrated heavily on the metal atom and the carbon chain and hardly on the phenyl ring. The computed anisotropy Δg increases when the atomic spin density is more localized on the metal center. The relative energy ΔE_{θ} of the different conformers, which corresponds to the difference in total energy between the most stable conformation and the conformer of a given θ value, is also plotted in Figure 6 as a red curve. Even though the shape of this curve is similar to that when Δg is plotted against θ , the maxima are not at the same θ values, allowing us to conclude that both Δg and ΔE_{θ} have to be taken into account to simulate the experimental measurements. Indeed, ionization potentials are thus correlated to the angle θ .

This conformational study was extended for each phenyl-ended system, and the resulting curves of the anisotropy and of the energy as a function of the dihedral angle θ are shown in Figure 6 (right) for $[\text{Ru-I-Ph}]^+$ and in Figure S3 of the Supporting Information for $[\text{Fe-2-Ph}]^+$ and $[\text{Ru-2-Ph}]^+$. As previously observed, the minima of anisotropy and energy are found for a value of θ close to 0° or 180° for both compounds. For the $[\text{Ru-I-Ph}]^+$ complex, some fluctuations of the energy

and the anisotropy are computed for θ close to 90° (see Figure 6). Guided by these energetic and anisotropic fluctuations of phenyl-containing systems, we can reconsider the computed anisotropy Δg values, taking into account the probability that a molecule exists in a certain conformation in the frozen solution. According to the Maxwell–Boltzmann distribution, this probability φ_{θ} is given by eq 1, where ΔE_{θ} is the difference

$$\varphi_{\theta} = \frac{e^{-\Delta E_{\theta}/(kT + \Delta E_{\text{solv}}(\theta))}}{\sum_{\theta} e^{-\Delta E_{\theta}/(kT + \Delta E_{\text{solv}}(\theta))}} \quad (1)$$

in energy between the most stable conformation and the conformer θ and $\Delta E_{\text{solv}}(\theta)$ is a solvation term specific for each complex (see Computational Details), which takes into account the energetic stabilization due to the solvent effects.

From this probability, the averaged values of the anisotropies $\langle \Delta g \rangle$ are calculated using eq 2 and are reported in Table 9. The

$$\langle \Delta g \rangle = \sum_{\theta} \Delta g_{\theta} \times \varphi_{\theta} \quad (2)$$

Table 9. Experimental Δg and Computed $\langle \Delta g \rangle$ Values for $[\text{Fe-}n\text{-Ph}]^+$ and $[\text{Ru-}n\text{-Ph}]^+$ for $n = 1, 2$

compd	exptl Δg	computed $\langle \Delta g \rangle^a$
$[\text{Fe-1-Ph}]^+$	0.489	0.483
$[\text{Fe-2-Ph}]^+$	0.454	0.445
$[\text{Ru-1-Ph}]^+$	0.229	0.273
$[\text{Ru-2-Ph}]^+$	0.420	0.333

^aSee eqs 1 and 2.

computed anisotropies $\langle \Delta g \rangle$ are much closer to the experimental values than the values reported in Table 8. The weakening of the anisotropy found in the $\text{R} = \text{H}$ series is also found for the $[\text{Fe-}n\text{-Ph}]^+$ systems, in accord with the decrease of the atomic spin density on the metal center. For the related ruthenium complexes, the lengthening of the carbon chain leads, both experimentally and theoretically, to an increase in Δg . This is due to the probabilities φ_{θ} of the conformations, with θ close to 90° for $[\text{Ru-I-Ph}]^+$ being much smaller than similar conformations of the other systems, resulting in a smaller Δg value (see Figure 6). A larger Δg value is calculated for $[\text{Ru-2-Ph}]^+$, for which this phenomenon does not occur.

The anisotropy tends to follow the metallic spin density, but some structures show the same spin density with a different computed anisotropy. Obviously, the atomic spin density is an average value that does not contain the information to understand this difference. The \mathbf{g} -tensor values and anisotropies

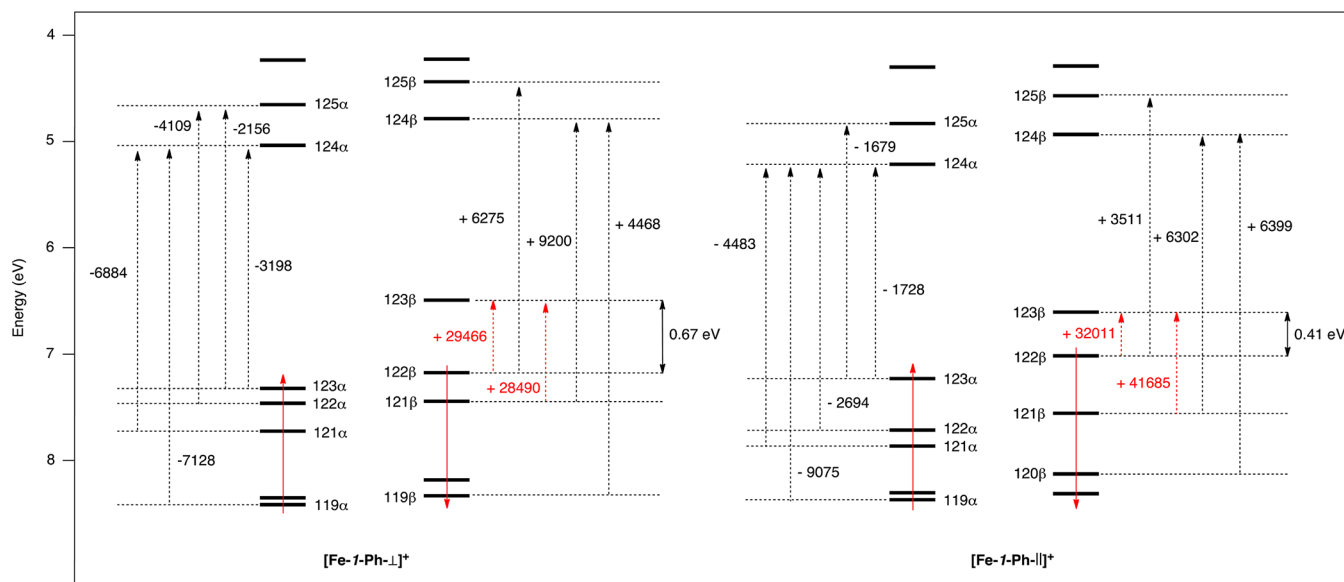


Figure 7. MO diagrams for the (\perp) and (\parallel) conformers of the $[\text{Fe-I-Ph}]^+$ complex. The numerical values of the $\Delta g^{\text{p,occ-vir}}$ contributions are given in ppm.

Δg depend on the environment of the unpaired electron. Ziegler and co-workers proposed a specific formalism to highlight this fact and thus to better understand the EPR properties.³² In this treatment, interest is focused on the deviation (Δg) of the computed \mathbf{g} -tensor components from the free electron value g_e ($g_e = 2.002319$). Each \mathbf{g} -tensor component (g_1 , g_2 , g_3 , and g_{iso}) is described as the sum of the free electron value plus several contributions.³³ For the complexes $[\text{Fe-}n\text{-Ph}]^+$ and $[\text{Ru-}n\text{-Ph}]^+$, the main contribution of the deviation of \mathbf{g} -tensor components (Δg) from the free electron value is the paramagnetic term Δg^{p} . This contribution can also be decomposed into several terms, which are the frozen core component ($\Delta g^{\text{p,core}}$) and the magnetic field induced couplings between occupied orbitals ($\Delta g^{\text{p,occ-occ}}$) and between occupied and virtual orbitals ($\Delta g^{\text{p,occ-vir}}$). We will focus on the $\Delta g^{\text{p,occ-vir}}$ contribution, which dominates the Δg value (deviation from the g_e value).³⁴

Molecular orbital diagrams of $[\text{Fe-I-Ph-}\perp]^+$ and $[\text{Fe-I-Ph-}\parallel]^+$ are shown in Figure 7 together with the principal contributions of the paramagnetic term $\Delta g^{\text{p,occ-vir}}$. These contributions are either positive or negative. The negative values are equivalent for both conformers. In contrast, a sizable change in intensities is found for the positive paramagnetic contributions corresponding to the coupling between the β -SOMO and β -SOMO-1 with the β -LUSO. Indeed, the two computed occupied-virtual mixing $122\beta \leftrightarrow 123\beta$ and $121\beta \leftrightarrow 123\beta$ increase from 29 466 and 28 490 ppm to 32 011 and 41 685 ppm, for the $[\text{Fe-I-Ph-}\perp]^+$ and $[\text{Fe-I-Ph-}\parallel]^+$ conformers, respectively. These values, which can be described as the magnetic coupling between spin-orbitals, include a term which is inversely proportional to their energy differences. Indeed, a large reduction of the β -SOMO- β -LUSO energy gap occurs upon rotation of the phenyl end group from $\theta = 179$ to 89° .

For $[\text{Ru-I-Ph}]^+$, important fluctuations of Δg are calculated for θ close to 90° , but the atomic spin densities are only weakly affected. As previously highlighted, these variations can be explained by some modification of the electronic structures in the SOMO-LUSO region. Indeed, the β -SOMO- β -LUSO energy gap varies between 0.26 and 0.34 eV for a change of

only 2° in the angle θ . In fact, other geometrical changes are associated with those small variations of the angle θ when close to 90° , mainly found in bending of the metal-carbon chain. The systems are unstable when linearity is imposed: geometry optimizations always lead to various distorted chains that induce better overlaps between the π -type phenyl and alkynyl networks and weaker overlaps between the metal and alkynyl parts. Most probably, this is due to the fact the ruthenium center is electronically saturated for θ far from 90° for this short chain. For θ close to 90° , due to the nonequivalence of the $d\pi_\perp$ and $d\pi_\parallel$ fragment orbitals of $[\text{Ru}(\text{dppe})\text{Cp}^*]^{2+}$, additional electron density would be transferred to the metal because of better orbital interactions. The ligand-to-metal back-bonding is reduced by geometrical distortions to avoid this excess of density. This is peculiar to $[\text{Ru-I-Ph}]^+$; for $n = 2, 3$, the electron density is more distributed over the chain and this phenomenon does not occur.

CONCLUSION

New organo-iron and -ruthenium complexes $\{\text{M}(\text{dppe})\text{Cp}^*\}-(\text{C}\equiv\text{C})_n\text{-R}$ containing C_2 , C_4 , and C_6 chains with different R end groups have been synthesized and characterized and their molecular structures determined. From the electrochemical investigations, some clear conclusions can be drawn: As expected, the iron complexes are easier to oxidize than their ruthenium analogues. Oxidation potentials are very sensitive to the chain length: the shorter the carbon chain, the easier the oxidation of the organometallic complex. Additionally, conclusions from the EPR investigations can be given: As expected, the anisotropy parameters in the iron complexes are larger overall than those in the ruthenium complexes. However, the effect of the carbon chain length seems to be negligible in some cases, as observed in the $[\text{M-}n\text{-SiMe}_3](\text{PF}_6)$ ($n = 1-3$) series, where the \mathbf{g} values are almost identical. This behavior is also computed for the $[\text{Ru-}n\text{-H}]^+$ series, even though the ruthenium spin density changes drastically. By studying more particularly the $[\text{M-}n\text{-Ph}]^+$ series, we are able to show theoretically that \mathbf{g} and Δg depend on the environment of the unpaired electron and that magnetic coupling between

occupied and virtual spin-orbitals provides the correct description of the evolution found within a series. EPR anisotropies do not correlate with metal spin density if the changes in the electronic structure are important.

Finally, with the more electron-rich R end groups, such as Au(PPh₃), the oxidation is easier. Analysis of the calculated atomic spin density of the oxidized system together with bond dissociation energies shows that radical reactions can occur on the even carbon atoms, labeled C₂, C₄, and C₆. This is tuned by the importance of the spin density and the steric hindrance of the considered carbon atom. Indeed, in the iron series, the stability of the iron(III) radical bearing ligands with four and six sp carbon atoms is in marked contrast with that of their alkynyl homologues. While the latter are stable in solution and in the solid state at 20 °C, the former decompose above -20 °C. This different behavior could be steric in origin, the two carbon atoms close to the metal center being more protected by the ancillary ligands. It can be also anticipated that the 17 e radical can change via a clean chemical process, since the ESR signal disappeared cleanly, no traces of other radicals being detected, except in the particular case of R = Au(PPh₃). Guided by these stimulating results, we are currently investigating the reactivities of these radical cations.

EXPERIMENTAL SECTION

General Procedures. Manipulations of air-sensitive compounds were performed under an argon atmosphere using standard Schlenk techniques or in an argon-filled Jacomex 532 drybox. Tetrahydrofuran (THF), diethyl ether, toluene, and pentane were dried and deoxygenated by distillation from sodium/benzophenone ketyl. Acetone was distilled from P₂O₅. Dichloromethane and dichloroethane were distilled under argon from P₂O₅ and then from Na₂CO₃. Methanol was distilled from dried magnesium turnings. The following compounds were prepared following published procedures: ferrocenium hexafluorophosphate (Fe(η⁵-C₅H₅)₂(PF₆)),¹⁶ FeCl(dppe)Cp*² and RuCl(dppe)Cp*.³ The complexes **Fe-2-SiMe₃**,⁶ **Ru-2-SiMe₃**,⁵ **Ru-2-Au(PPh₃)₃**,⁵ **Ru-3-SiMe₃**,¹⁰ and **Ru-3-Au(PPh₃)₃**¹⁰ were prepared following the cited procedures. Potassium *tert*-butoxide (ACROS) was used without further purification. Infrared spectra were obtained in KBr disks with a Bruker IFS28 FTIR infrared spectrophotometer (4000–400 cm⁻¹). UV–visible spectra were recorded on a Varian CARY 5000 spectrometer. ¹H, ¹³C, and ³¹P NMR spectra were recorded on Bruker DPX200, Avance 300, and Avance 500 NMR multinuclear spectrometers at ambient temperature, unless otherwise noted. Chemical shifts are reported in ppm (δ) relative to tetramethylsilane (TMS), using the residual solvent resonances as internal references. Coupling constants (*J*) are reported in hertz (Hz), and integrations are reported as numbers of protons. The following abbreviations are used to describe peak patterns: br = broad, s = singlet, d = doublet, dd = doublet of doublets, t = triplet, q = quartet, m = multiplet. ¹H and ¹³C NMR peak assignments are supported by the use of COSY, HMQC, and HMBC experiments. High-resolution mass spectra (HRMS) were recorded with a high-resolution ZabSpec TOF VG analytical spectrometer operating in the ESI+ mode, at the Centre Régional de Mesures Physiques de l'Ouest (CRMPO), Rennes, France, or with a Bruker MicroTOF spectrometer at the University of Waikato, Waikato, New Zealand. Poly(ethylene glycol) (PEG) was used as an internal reference, and dichloromethane was used as solvent. All mass measurements refer to peaks for the most abundant isotopic combination (¹H, ¹²C, ³¹P, ⁵⁶Fe, ¹⁰²Ru). EPR spectra were recorded on a Bruker EMX-8/2.7 (X-band) spectrometer. Elemental analyses of the iron compounds were conducted on a Thermo-FINNIGAN Flash EA 1112 CHNS/O analyzer by the Microanalytical Service of the CRMPO at the University of Rennes 1, Rennes, France, and those of the ruthenium complexes at Campbell Microanalytical Laboratory, Dunedin, New Zealand.

Synthesis of Fe(C≡CC≡CPh)(dppe)Cp* (Fe-2-Ph). To a suspension of FeCl(dppe)Cp* (100 mg, 0.16 mmol) and NaBPh₄ (66 mg, 0.19 mmol) in triethylamine (15 mL) was added a solution of HC≡CC≡CPh³⁵ (24 mg, 0.19 mmol) in THF (1 mL). The mixture turned slowly from dark green to orange. After one night at room temperature, ^tBuOK (excess) was added to the solution before removal of the solvent under reduced pressure. The solid residue was then extracted with toluene (3 × 10 mL), and the solvent was removed under reduced pressure. The residue was extracted a second time with diethyl ether (3 × 10 mL), and after removal of the solvent under reduced pressure, the resulting orange powder was dried under vacuum to afford Fe(C≡CC≡CPh)(dppe)Cp* (**Fe-2-Ph**; 97 mg, 85%). Anal. Calcd for C₄₆H₄₄FeP₂: C, 77.31; H, 6.21. Found: C, 76.59; H, 6.18. IR (KBr): ν(C≡C) 2150, 2007, 1987 cm⁻¹. ¹H NMR (C₆D₆, 300 MHz): δ 1.45 (s, 15H, Cp*), 1.77, 2.58 (2 × m, 4H, PCH₂), 6.87–8.02 (m, 25H, Ph). ¹³C NMR (C₆D₆, 75 MHz, ppm): δ 8.89 (s, C₅Me₃), 28.79–29.91 (m, dppe), 59.70 (s, C≡CC≡CPh), 80.98 (s, C≡CC≡CPh), 87.26 (s, C₅Me₃), 100.06 (s, C≡CC≡CPh), 124.42–137.88 (m, Ph), 144.74 (t, ²J_{CP} = 38 Hz, C≡CC≡CPh). ³¹P NMR (C₆D₆, 121 MHz): δ 100.2 (s). ES-MS (*m/z*): calcd for C₄₆H₄₄FeP₂ 714.2268, found 714.2275 [M]⁺.

Synthesis of Ru(C≡CC≡CPh)(dppe)Cp* (Ru-2-Ph). A methanolic (7 mL, containing 1% of distilled H₂O) suspension of RuCl(dppe)Cp* (100 mg, 0.15 mmol), Me₃SiC≡CC≡CPh³⁶ (33 mg, 0.16 mmol), KF (10 mg, 0.16 mmol), and DBU (2 drops) was heated under reflux. After 1 h, the mixture was cooled and the yellow-green precipitate filtered off and washed with cold MeOH. The resulting powder was then dissolved in DCM (containing 5% of NEt₃) and the solution passed through a basic alumina column with the same solvent as eluent. The yellow band was collected and the solvent removed to give Ru(C≡CC≡CPh)(dppe)Cp* (**Ru-2-Ph**; 99 mg, 87%) as a bright yellow powder. Anal. Calcd for C₄₆H₄₄P₂Ru: C, 72.71; H, 5.84. Found: C, 72.59; H, 6.00. IR (CH₂Cl₂): ν(C≡C) 2153, 2016 cm⁻¹. ¹H NMR (C₆D₆, 600 MHz): δ 1.59 (s, 15H, Cp*), 1.84, 2.60 (2 × m, 4H, PCH₂), 6.87–7.89 (m, 25H, Ph). ¹³C NMR (C₆D₆, 150 MHz, ppm): δ 9.88 (s, C₅Me₃), 29.23–29.54 (m, dppe), 62.98, 82.34, 92.19 (s, C≡C), 93.10 (s, C₅Me₃), 125.47–138.55 (m, Ph and C₄). ³¹P NMR (C₆D₆, 121 MHz): δ 80.3 (s). ES-MS (*m/z*): calcd for C₄₆H₄₅P₂Ru 761.2040, found 761.2065 [M + H]⁺.

Synthesis of Fe(C≡CC≡CAu(PPh₃))(dppe)Cp* (Fe-2-Au(PPh₃)). To a suspension of Fe(C≡CC≡CSiMe₃)(dppe)Cp* (7) (400 mg, 0.56 mmol) in THF (10 mL) was added a solution of NaOMe (from Na (65 mg, 2.81 mmol) in methanol (10 mL)). After the mixture was stirred for 20 min at room temperature, AuCl(PPh₃)₃ (278 mg, 0.56 mmol) was added, upon which the solution turned dark red. After 4 h, the orange precipitate was filtered off and washed with cold MeOH (3 × 10 mL) to afford Fe(C≡CC≡CAu(PPh₃))(dppe)Cp* as an orange powder ([**Fe-2-Au(PPh₃)**]; 452 mg, 74%). Anal. Calcd for C₅₈H₅₄AuFeP₃: C, 63.52; H, 4.96. Found: C, 63.10; H, 5.23. IR (CH₂Cl₂): ν(C≡C) 2069, 1969 cm⁻¹. ¹H NMR (C₆D₆, 300 MHz): δ 1.53 (s, 15H, Cp*), 1.83, 2.73 (2 × m, 4H, PCH₂), 6.88–8.19 (m, 35H, Ph). ¹³C NMR (C₆D₆, 150 MHz, ppm): δ 10.45 (s, C₅Me₃), 30.22–31.39 (m, dppe), 88.25 (s, C₅Me₃), 88.84 (s), 94.18 (s), 104.06 (s), 123.26 [t, ²J_{CP} = 40 Hz, C≡CC≡CAu(PPh₃)], 126.30–140.40 (m, Ph). ³¹P NMR (C₆D₆, 121 MHz): δ 100.0 (s, dppe), 42.0 (s, PPh₃). ES-MS (*m/z*): calcd for C₅₈H₅₄AuFeP₃ 1096.2453, found 1096.2525 [M]⁺.

Synthesis of Fe(C≡CC≡CCSiMe₃)(dppe)Cp* (Fe-3-SiMe₃). To a stirred solution of Fe(C≡CC≡CAu(PPh₃))(dppe)Cp* (**Fe-2-Au(PPh₃)**; 250 mg, 0.23 mmol) in a 1/1 mixture of THF and triethylamine (24 mL) was added IC≡CSiMe₃ (128 mg, 0.57 mmol) followed immediately by Pd(PPh₃)₄ (26 mg, 0.023 mmol) and CuI (8 mg, 0.041 mmol). The solution was stirred in the dark at room temperature overnight before solvent was removed under reduced pressure. The residue was extracted with triethylamine and directly loaded onto a basic alumina column which was eluted with triethylamine/hexane (1/1); the orange band was collected to afford Fe(C≡CC≡CCSiMe₃)(dppe)Cp* (**Fe-3-SiMe₃**; 93 mg, 55%) as an orange powder. Anal. Calcd for C₄₅H₄₈FeP₂Si: C, 73.56; H, 6.58. Found: C, 73.80; H, 7.47. IR (CH₂Cl₂): ν(C≡C) 2092, 1952 cm⁻¹.

Table 10. Crystal Data and Refinement Details for Fe-2-Ph, Ru-2-Ph, Fe-2-Au(PPh₃), Fe-3-SiMe₃, Ru-3-SiMe₃, and Ru-3-Au(PPh₃)

	Fe-2-Ph	Ru-2-Ph	Fe-2-Au(PPh ₃)	Fe-3-SiMe ₃	Ru-3-SiMe ₃	Ru-3-Au(PPh ₃)
formula	C ₄₆ H ₄₄ FeP ₂	C ₄₆ H ₄₄ P ₂ Ru	C ₅₈ H ₅₄ AuFeP ₃ ·3CH ₂ Cl ₂	C ₄₅ H ₄₈ FeP ₂ Si	C ₄₅ H ₄₈ RuP ₂ Si _{0.25} C ₆ H ₁₄	C ₆₀ H ₅₄ AuP ₃ Ru
mol wt	714.60	759.82	1349.82	734.71	801.48	1165.98
T (K)	100(2)	110(2)	100(2)	100(2)	150(2)	150(2)
cryst syst	monoclinic	monoclinic	triclinic	monoclinic	monoclinic	triclinic
space group	P2 ₁ /c	P2 ₁ /c	P $\bar{1}$	C2/c	C2/c	P $\bar{1}$
a (Å)	10.6050(3)	10.6501(4)	12.6624(5)	47.893(3)	48.476(14)	10.523(1)
b (Å)	35.2980(11)	35.7310(13)	14.5461(6)	17.882(2)	18.052(6)	11.313(1)
c (Å)	10.3375(4)	10.2532(3)	16.4850(7)	20.3130(10)	20.193(6)	23.935(3)
α (deg)			93.418(4)	90.00	90.00	96.928(3)
β (deg)	107.578(1)	107.285(3)	102.305(4)	102.660(10)	102.174(5)	97.902(3)
γ (deg)			99.647(4)	90.00	90.00	110.162(3)
V (Å ³)	3689.0(2)	3725.5(2)	2910.3(2)	16974(2)	17273(9)	2605.8(5)
Z	4	4	2	16	16	2
ρ_{calcd} (g cm ⁻³)	1.287	1.355	1.540	1.150	1.233	1.486
cryst size (mm)	0.36 × 0.27 × 0.24	0.51 × 0.17 × 0.04	0.33 × 0.24 × 0.15	0.55 × 0.04 × 0.03	0.35 × 0.07 × 0.05	0.26 × 0.14 × 0.13
F(000)	1504	1576	1354	6208	6696	1164
radiation	Mo K α	Mo K α	Mo K α	Cu K α	Mo K α	Mo K α
abs coeff (mm ⁻¹)	0.528	0.538	3.16	4.04	0.494	3.23
θ range (deg)	3.46–27.47	2.63–32.63	3.56–30.00	3.32–67.18	1.21–27.59	1.75–31.00
hkl range	–13 to +13 –45 to +45 –13 to +6	–15 to +16 –53 to +53 –15 to +15	–17 to +17 –20 to +20 –15 to +23	–56 to +55 –20 to +20 –23 to +15	–63 to 61 –23 to 23 –26 to 26	–15 to +15 –16 to +16 –34 to +34
N _{tot}	54 427	58 066	35 043	43 988	68 019	30 112
N (R _{int})	8379 (0.032)	13 019 (0.048)	16 932 (0.051)	14 952 (0.129)	19 746 (0.072)	15 458 (0.035)
N _o	7641	9594	11 588	7101	13 480	11 359
no. of restraints/params	0/447	0/447	0/678	114/960	16/925	0/591
R1 (I > 2 σ (I))	0.029	0.037	0.047	0.062	0.060	0.047
wR2 (all data)	0.074	0.081	0.105	0.174	0.157	0.124
goodness of fit/F ²	1.036	0.94	0.977	0.945	1.019	1.107
largest diff peak, hole (e Å ⁻³)	0.421, –0.334	1.327, –0.384	3.499, –2.764	0.763, –0.792	1.501, –0.74	2.65, –0.654

¹H NMR (C₆D₆, 300 MHz): δ 0.13 (s, 9H, SiMe₃), 1.37 (s, 15H, Cp*), 1.69, 2.42 (2 × m, 4H, PCH₂), 6.98–7.85 (m, 20H, Ph). ¹³C NMR (C₆D₆, 150 MHz, ppm): δ 0.35 (s, SiMe₃), 10.12 (s, C₅Me₃), 30.23–31.08 (m, dppe), 47.06, 69.29, 77.18, 94.34, 100.95 (s, C≡C), 89.31 (s, C₃Me₃), 127.53–138.60 (m, Ph), 151.07 (t, ²J_{PC} = 38 Hz, C₄). ³¹P NMR (C₆D₆, 121 MHz): δ 97.9 (s). ES-MS (*m/z*): calcd for C₄₅H₄₈FeP₂Si 734.2350, found 734.2388 [M]⁺.

X-ray Crystallography. Single crystals suitable for X-ray structure determination were obtained as follows: (i) **Fe-2-Ph**, slow diffusion of pentane in a toluene solution of the complex; (ii) **Ru-2-Ph**, slow diffusion of hexane into dichloromethane solution of the complex; (iii) **Fe-2-Au(PPh₃)** and **Ru-3-Au(PPh₃)**, slow evaporation of a dichloromethane solution of the complex; (iv) **Fe-3-SiMe₃** and **Ru-3-SiMe₃**, slow diffusion of hexane into triethylamine solutions of the complexes. Crystal data and data collection and refinement parameters are given in Table 10. Full spheres of diffraction data were measured using CCD area-detector instrumentation equipped with monochromatic Mo or Cu K α radiation (λ = 0.710 73 or 1.541 78 Å). Anisotropic displacement parameter forms were refined for the non-hydrogen atoms. All H atoms were added at calculated positions and refined by use of a riding model with isotropic displacement parameters based on those of the parent atom. Neutral atom complex scattering factors were used; computation used the SHELXL 97 program.³⁷

Computational Details. Calculations were performed with the ADF2010.02 package.³⁸ Electron correlation was treated within the local density approximation (LDA) in the Vosko–Wilk–Nusair parametrization.³⁹ The nonlocal corrections (GGA) of Becke and Perdew were added to the exchange and correlation energies, respectively.⁴⁰ The analytical gradient method implemented by Versluis and Ziegler was used.⁴¹ The standard ADF TZP basis set

was used for the geometry optimizations of [Fe-*n*R]^{0/+} and [Ru-*n*R]^{0/+}, with *n* = 1–3 and R = H, Ph and with *n* = 2 and R = SiMe₃. Explicitly, this basis set is a triple- ξ STO basis set for the valence shells augmented with a 2p polarization function for H, a 3d polarization function for C, P, and Si, a 4p polarization function for Fe, and a 5p polarization function for Ru, respectively. Orbitals up to 1s, 2p, 3p, and 4p were kept frozen for C, P, Si, Fe, and Ru, respectively. For [Fe-2-Au(PPh₃)]^{0/+} and [Ru-2-Au(PPh₃)]^{0/+}, a relativistic zeroth-order regular approximation (ZORA) was applied using the ZORA/TZP adapted basis set (frozen core: Au 1s–4f).⁴² The geometries were fully optimized without constraints (C₁ symmetry), and convergence criteria used were more drastic than default criteria (energy change <0.0005 hartree, atomic position displacement <0.005 Å). The bonding energies and Cartesian coordinates of each structure are given in Table S12 (Supporting Information). In order to evaluate the effect of rotation of the phenyl end groups in the [Fe-*n*-Ph]⁺ and [Ru-*n*-Ph]⁺ series (*n* = 1, 2), a sequence of constrained-geometry optimizations were carried out. The dihedral θ (θ = Cp* centroid–M–C_{ipso}–C_{ortho}) cannot be fixed directly, since one of the geometrical points which defines it is the centroid of five atoms. A combination of dihedral angles between atoms (P(dppe), M, C(Ph)) was used to obtain θ values that can diverge from 1° from the expected value. Computed EPR properties given in Table 8 and Tables S4–S6 and 11 (Supporting Information) were performed using the ESR procedure developed by van Lenthe and co-workers.^{27a,43} The g-tensor components were obtained from self-consistent spin-restricted DFT calculations after incorporating the relativistic spin–orbit coupling by first-order perturbation theory from a ZORA Hamiltonian. Calculations did not take spin-polarization effects into account. For these calculations, the nonlocal correction of Adamo–Barone and of

Perdew–Burke–Ernzerhof (mPBE) were added to the exchange and correlation energies, respectively,⁴⁴ and the basis set was expanded for Fe and Ru, where orbitals up to 2p and 3d were kept frozen, respectively. Deviations (Δg) of the computed g-tensor components from the free electron value g_e , shown in Figure 7, were computed using the EPR module developed by Ziegler and co-workers.³² Scalar relativistic effects were included employing relativistic frozen core potentials in conjunction with the first-order Pauli Hamiltonian.⁴⁵ Evaluation of the g-tensors was obtained with spin-unrestricted calculations using the gradient-corrected BP86 functional,⁴⁰ and the basis set was expanded for Fe and Ru, where orbitals up to 2p and 3d were kept frozen, respectively.

ΔE_θ is the energetic difference between the most stable conformation and a conformer θ . The $\Delta E_{\text{solv}}(\theta)$ term, used in eq 1, reports the energetic stabilization due to the solvent. To address solvation effects, the conductor-like screening model (COSMO)⁴⁶ was used with a dielectric constant simulating dichloromethane solvent. The geometries were not relaxed because of the prohibitive computational cost. To evaluate the degree of this approximation, we have performed full COSMO geometry optimizations of the two conformers of $[\text{Fe-1-Ph}]^+$ with θ equal to 75 and 180°. The difference in energy between the two compounds is 0.096 eV when 0.138 eV is calculated between the two conformers relaxed under vacuum. The difference of solvation calculated by COSMO is thus 0.043, and it was estimated to be 0.068 eV on the basis of nonrelaxed structures. The geometries are slightly different with optimized angles θ of 74.3 and 178.1° in comparison to 74.2 and 178.7° under vacuum. The Δg values are thus also slightly modified with 0.695 instead of 0.683 for $\theta \approx 75^\circ$ and 0.298 instead of 0.266 for $\theta \approx 180^\circ$. Overall, these changes will marginally affect our results, since they will most probably be on the same order of magnitude for all of the rotamers.

■ ASSOCIATED CONTENT

■ Supporting Information

CIF files, figures, and tables giving all crystallographic data and selected bond distances and bond angles for **Fe-2-Ph**, **Ru-2-Ph**, **Fe-2-Au(PPh₃)**, **Fe-3-SiMe₃**, **Ru-3-SiMe₃**, and **Ru-3-Au(PPh₃)**, selected X-ray structural parameters, energies and Mulliken decomposition of **Ru-2-R** MOs, calculated EPR data, atomic spin densities, and dipole moments for $[\text{Ru-}n\text{-Ph}]^+$ and $[\text{Fe-}n\text{-Ph}]^+$ ($n = 1, 2$), DFT MO diagrams of **Fe-}n\text{-H}** ($n = 1\text{--}3$) and **Ru-2-R**, bond dissociation energy decomposition of $\text{C}_4\text{-R}$ for $[\text{M-2-R}]^+$, and Cartesian coordinates of all calculated geometries. This material is available free of charge via the Internet at <http://pubs.acs.org>. Full details of the structure determinations have also been deposited with the Cambridge Crystallographic Data Centre as CCDC 887627, 804391, 885401, 881307, 885402, and 830957. Copies of this information may be obtained free of charge from The Director, CCDC, 12 Union Street, Cambridge CB2 1EZ, U.K. (fax, +44-1223-336-033; e-mail, deposit@ccdc.cam.ac.uk; web, <http://www.ccdc.cam.ac.uk>).

■ AUTHOR INFORMATION

Corresponding Author

*E-mail: claude.lapinte@univ-rennes1.fr (C.L.); kcostuas@univ-rennes1.fr (K.C.).

Present Address

^{||}CMCA, University of Western Australia, Crawley, Western Australia 6009, Australia.

Notes

The authors declare no competing financial interest.

■ ACKNOWLEDGMENTS

The MNERT (Ph.D. grants to A.B. and F.G.) and UEB (travel grant to A.B.) are acknowledged for financial support. We thank the Centre National de la Recherche Scientifique and the Australian Research Council for support of this work. Frédéric Justaud is warmly acknowledged for EPR assistance. We thank Johnson Matthey plc, Reading, U.K., for a generous loan of $\text{RuCl}_3 \cdot n\text{H}_2\text{O}$. This work was performed using HPC resources from GENCI-CINES and GENCI-IDRIS (Grant 2011-80649).

■ REFERENCES

- (1) Szafert, S.; Gladysz, J. A. *Chem. Rev.* **2006**, *106*, PR1–PR33.
- (2) Roger, C.; Hamon, P.; Toupet, L.; Raba , H.; Saillard, J.-Y.; Hamon, J.-R.; Lapinte, C. *Organometallics* **1991**, *10*, 1045–1054.
- (3) Bruce, M. I.; Ellis, B. G.; Low, P. J.; Skelton, B. W.; White, A. H. *Organometallics* **2003**, *22*, 3184–3198.
- (4) Denis, R.; Toupet, L.; Paul, F.; Lapinte, C. *Organometallics* **2000**, *19*, 4240–4251.
- (5) Bruce, M. I.; Ellis, B. G.; Gaudio, M.; Lapinte, C.; Melino, G.; Paul, F.; Skelton, B. W.; Smith, M. E.; Toupet, L.; White, A. H. *Dalton Trans.* **2004**, 1601–1609.
- (6) Coat, F.; Guillevic, M.-A.; Toupet, L.; Paul, F.; Lapinte, C. *Organometallics* **1997**, *16*, 5988–5998.
- (7) Paul, F.; Meyer, W. E.; Toupet, L.; Jiao, H.; Gladysz, J. A.; Lapinte, C. *J. Am. Chem. Soc.* **2000**, *122*, 9405–9414.
- (8) Paul, F.; Lapinte, C. *Coord. Chem. Rev.* **1998**, *178–180*, 427–505.
- (9) Szafert, S.; Paul, F.; Meyer, W. E.; Gladysz, J. A.; Lapinte, C. *Chimie* **2008**, *11*, 693–701.
- (10) Bruce, M. I.; Cole, M. L.; Parker, C. R.; Skelton, B. W.; White, A. H. *Organometallics* **2008**, *27*, 3352–3367.
- (11) Hamon, P.; Toupet, L.; Hamon, J.-R.; Lapinte, C. *Organometallics* **1996**, *15*, 10–12.
- (12) Paul, F.; Toupet, L.; Th pot, J.-Y.; Costuas, K.; Halet, J.-F.; Lapinte, C. *Organometallics* **2005**, *24*, 5464–5478.
- (13) Paul, F.; Ellis, B. E.; Bruce, M. I.; Toupet, L.; Roisnel, T.; Costuas, K.; Halet, J.-F.; Lapinte, C. *Organometallics* **2006**, *25*, 649–665.
- (14) Le Narvor, N.; Toupet, L.; Lapinte, C. *J. Am. Chem. Soc.* **1995**, *117*, 7129–7138.
- (15) Connelly, N. G.; Gamasa, M. P.; Gimeno, J.; Lapinte, C.; Lastra, E.; Maher, J. P.; Le Narvor, N.; Rieger, A. L.; Rieger, P. H. *J. Chem. Soc., Dalton Trans.* **1993**, 2575–2578.
- (16) Connelly, N. G.; Geiger, W. E. *Chem. Rev.* **1996**, *96*, 877–910.
- (17) Bruce, M. I.; Burgun, A.; Gendron, F.; Grelaud, G.; Halet, J.-F.; Skelton, B. W. *Organometallics* **2011**, *30*, 2861–2868.
- (18) See, for example, for recent work: (a) Fitzgerald, E. C.; Ladjarafi, A.; Brown, N. J.; Collison, D.; Costuas, K.; Edge, R.; Halet, J.-F.; Justaud, F.; Low, P. J.; Meghezzi, H.; Roisnel, T.; Whiteley, M. W.; Lapinte, C. *Organometallics* **2011**, *30*, 4180–4195. (b) Costuas, K.; Cadot, O.; Justaud, F.; Le Stang, S.; Paul, F.; Monari, A.; Evangelisti, S.; Toupet, L.; Lapinte, C.; Halet, J.-F. *Inorg. Chem.* **2011**, *50*, 12601–12622. (c) Fox, M. A.; Le Guennic, B.; Roberts, R. L.; Brue, D. A.; Yufit, D. S.; Howard, J. A. K.; Manca, G.; Halet, J.-F.; Hartl, F.; Low, P. J. *J. Am. Chem. Soc.* **2011**, *133*, 18433–18446. (d) Roberts, H. N.; Brown, N. J.; Edge, R.; Fitzgerald, E. C.; Ta, Y. T.; Collison, D.; Low, P. J.; Whiteley, M. W. *Organometallics* **2012**, DOI: 10.1021/om3005756.
- (19) The largest atomic basis set (QZ4P) and spin–orbit coupling calculations strongly improve the results, but the computational cost is too high to carry out this type of calculations on the whole set of molecules studied.
- (20) Rousseau, R.; Low, P. J. *Organometallics* **2001**, *20*, 4502–4509.
- (21) Dahlenburg, L.; Weib, A.; Bock, M.; Zahl, A. *J. Organomet. Chem.* **1997**, *541*, 465–471.
- (22) Costuas, K.; Rigaut, S. *Dalton Trans.* **2011**, *40*, 5621–5658.
- (23) (a) Morokuma, K. *J. Chem. Phys.* **1971**, *55*, 1236–1244. (b) Ziegler, T.; Rauk, A. *Theor. Chim. Acta* **1977**, *46*, 1–10.

(24) (a) Maurer, J.; Linseis, M.; Sarkar, B.; Schwederski, B.; Niemyer, M.; Kaim, W.; Zališ, S.; Anson, C.; Zabel, M.; Winter, R. F. *J. Am. Chem. Soc.* **2008**, *130*, 259–268. (b) Man, W. Y.; Xia, J.-L.; Brown, N. J.; Farmer, J. D.; Yufit, D. S.; Howard, J. A. K.; Liu, S. H.; Low, P. J. *Organometallics* **2011**, *30*, 1852–1858.

(25) Paul, F.; Toupet, L.; Roisnel, T.; Hamon, P.; Lapinte, C. C. R. *Chim.* **2005**, *8*, 1174–1185.

(26) (a) EPR Parameters, Methodological Aspects. In *Calculation of NMR and EPR parameters. Theory and Applications*, 1st ed.; Kaupp, M., Bühl, M., Malkin, V. G., Eds.; Wiley-VCH: Weinheim, Germany, 2004. (b) Boguslawski, K.; Jacob, C. R.; Reiher, M. *J. Chem. Theory Comput.* **2001**, *7*, 2740–2752.

(27) (a) van Lenthe, E.; van der Avoird, A.; Wormer, P. E. S. *J. Chem. Phys.* **1998**, *108*, 4783–4796. (b) Pyykkö, P. *Chem. Rev.* **1988**, *88*, 563–594.

(28) H, SiMe₃, and Au(PPh₃) are conical fragments for which the rotation does not affect the total energies and electronic structures.

(29) (a) Engstrom, M.; Vahtras, O.; Agren, H. *Chem. Phys.* **1999**, *243*, 263–271. (b) Mattar, S. M.; Sanford, J. *Chem. Phys. Lett.* **2006**, *425*, 148–153.

(30) Gauthier, N.; Tchouar, N.; Justaud, F.; Argouarch, G.; Cifuentes, M. P.; Toupet, L.; Touchard, D.; Halet, J.-F.; Rigaut, S.; Humphrey, M. G.; Costuas, K.; Paul, F. *Organometallics* **2009**, *28*, 2253–2266.

(31) The curvature of the carbon chain and the nonsymmetrical environment of the metal center lead to nonsymmetrical curves (see Figure 7).

(32) (a) Schreckenbach, G.; Ziegler, T. *J. Phys. Chem. A* **1997**, *101*, 3388–3399. (b) Patchkovskii, S.; Ziegler, T. *J. Phys. Chem. A* **2001**, *105*, 5490–5497.

(33) $\mathbf{g} = g_e \delta + \Lambda g^{\text{KE}} + \Lambda g^{\text{MV}} + \Lambda g^{\text{Darwin}} + \Lambda g^{\text{d}} + \Lambda g^{\text{p}}$. Here Λg^{KE} , Λg^{MV} , and $\Lambda g^{\text{Darwin}}$ are relativistic corrections arising from the kinetic energy, mass-velocity, and Darwin terms and Λg^{d} and Λg^{p} are the diamagnetic and paramagnetic contributions to the \mathbf{g} -tensor, respectively.

(34) It should be noted that the $\Lambda g^{\text{p,occ-vir}}$ contribution ignores spin-polarization effects and relativistic contributions apart from the spin-orbit coupling and should therefore be used only as a qualitative tool rather than for quantitative predictions of \mathbf{g} -tensor components.

(35) West, K.; Wang, C.; Batsanov, A. S.; Bryce, M. R. *J. Org. Chem.* **2006**, *71*, 8541–8544.

(36) Fiandanese, V.; Bottalico, D.; Marchese, G.; Punzi, A. *Tetrahedron Lett.* **2003**, *44*, 9087–9090.

(37) Sheldrick, G. M. *Acta Crystallogr.* **2008**, *A64*, 112–122.

(38) (a) te Velde, G.; Bickelhaupt, F. M.; Baerends, E. J.; Fonseca Guerra, C.; van Gisbergen, S. J. A.; Snijders, J. G.; Ziegler, T. *J. Comput. Chem.* **2001**, *22*, 931–967. (b) *ADF2010.02*; SCM, Theoretical Chemistry, Vrije Universiteit: Amsterdam, The Netherlands (www.scm.com).

(39) Vosko, S. H.; Wilk, L.; Nusair, M. *Can. J. Phys.* **1980**, *58*, 1200–1211.

(40) (a) Becke, A. D. *Phys. Rev. A* **1988**, *38*, 3098–3100. (b) Perdew, J. P. *Phys. Rev. B* **1986**, *33*, 8822–8824.

(41) Versluis, L.; Ziegler, T. *J. Chem. Phys.* **1988**, *88*, 322–328.

(42) (a) van Lenthe, E.; Ehlers, A. E.; Baerends, E. J. *J. Chem. Phys.* **1999**, *110*, 8943–8953. (b) van Lenthe, E.; Baerends, E. J. *J. Comput. Chem.* **2003**, *24*, 1142–1156.

(43) (a) van Lenthe, E.; van der Avoird, A.; Wormer, P. E. S. *J. Chem. Phys.* **1997**, *107*, 2488–2498. (b) Autschbach, J.; Pritchard, B. *Theor. Chem. Acc.* **2011**, *129*, 453–466.

(44) (a) Adamo, C.; Barone, V. *J. Chem. Phys.* **2002**, *116*, 5933–5940. (b) Perdew, J. P.; Burke, K.; Ernzerhof, M. *Phys. Rev. Lett.* **1996**, *77*, 3865–3868.

(45) Ziegler, T.; Tschinke, V.; Baerends, E. J.; Snijders, J. G.; Ravenek, W. *J. Phys. Chem.* **1989**, *93*, 3050–3056.

(46) (a) Pye, C. C.; Ziegler, T. *Theor. Chem. Acc.* **1999**, *101*, 396–408. (b) Klamt, A. *J. Phys. Chem.* **1995**, *99*, 2224–2235.